ROTATIONAL & TRANSLATIONAL ELECTRICAL TRAPPING OF SUPERELLIPSOIDAL PARTICLE IN NONUNIFORM FIELD

by

Zhaonian Jia

A thesis submitted to Johns Hopkins University in conformity with the requirements for the degree of Master of Science in Engineering

Baltimore, Maryland

April 2019

ABSTRACT

Research on colloidal particle suspensions has become important for a wide range of applications. In this work, a new type of electrode is designed and produced through micro-fabrication. We used the new electrode to manipulate a single superellipsoidal particle, providing complete control on a particle position and orientation as a function of field frequency and strength. The interacting force and torque on the superellipsoidal particle due to its interaction with the AC electric field are investigated and directly calculated. Furthermore, we introduce the concept of stiffness to describe the strength of the restriction (in position and orientation) generated by the electric field on the particle. Understanding the magnitude of the stiffness, and its dependence on the field frequency and amplitude enables a direct and precise control of particle position and orientation within nonuniform fields.

Committee: Prof. Michael A. Bevan (academic advisor, ChemBE)

Prof. Joelle Frechette (ChemBE)

TABLE OF CONTENTS

LIST OF FIGURES

1. INTRODUCTION

Colloids are particles within a range of size that are suspended in a fluid phase. The typical size range of colloidal particle is between 10 nm to several microns.[1] Between this size range, the particles are small enough to be affected by thermal energy, but also large enough that optical methods can track and quantify its position, orientation, and relative motion precisely. There are many different applications of colloids, such as inks, paints, and 3D painting material.[1] Colloidal particles are not only widely existing in nature, but they can also be fabricated with extremely precision. [2,3] It is possible to produce a large number of particles with tunable shape and remarkable uniformity. Moreover, interaction between particles, particle-field, and particle-substrate can be tuned by changing the surface properties of particles. [4] The properties and techniques described above make colloidal particles as a suitable model to study different system in cement, [5] foams [6] and virus.[7] One of the most widely studied model is the hard-sphere system; although this model is used to study particle dynamics and the assembly of multiple particle systems, there are anisotropic (surface and shape) colloids with more complicated behavior and actuation (force and torque) than uniform spherical colloids. Anisotropic particles could have different properties in different directions, which not only include the asymmetry on surface and shape, but also it can be composed of a mixture of materials, roughness, and features with unique functionalities.[8-10] Researchers have different ways to classify the anisotropic particles.[8-10] Here, we classify the anisotropic particles into the

following types: shape asymmetry, patchy particles (surface anisotropy), anisotropic material compartmentalization, internally structured particles, and complex architectures which is the combination of the previous properties. In our research, we limit the analysis to the uniaxial anisotropic particles. Axisymmetric colloidal particles with different shapes such as rods, disks, fibers, tubes, dumbbell-shapes, acorn-shapes, sheets and spheroids have been prepared through a variety of methods. [2] As demonstrated in several studies, uniform particles with non-spherical shape change the individual[11] and collective [12] behavior of colloidal system. Non-spherical particles are good models for the study of cell and virus which provides unique and advanced abilities that are difficult to reach with spherical particles.[Ref] Recent studies also show that shape is an important parameter for drug delivery carriers.[13] For instance, rod-like particles show different endocytosis properties in Hela cells compared to spheres.[14] Muro *et al*.[15] showed that using polystyrene (PS) particles exhibit longer circulation and higher targeting than spherical particles.

New technological processes at micro- and nano-scales generally depend on the ability to control and manipulate characteristics single/multiple objects. Jun Ge *et al*. describe a temperature and electric field dual-stimulus responsive nanoparticle system which can be used in programmed drug delivery.[16] Many researches focused on magnetic nanoparticles and demonstrated that magnetic nanoparticles with good stability can be useful for effective separation of catalysts, nuclear waste, biochemical products and cells [17-19]. One important aspect of these techniques is the developing of 'touchless' technologies, which intends to apply gentle forces/torques that are

generated from the external field gradient to manipulate the position and orientation of these microscopic particles.

In recent years, several techniques have been developed using this concept including optical tweezers,[20] electric tweezers,[21] dielectrophoresis,[22] magnetic tweezers,[23] and thermal tweezers.[24] Such methods are based on the understanding of the interactions between the colloidal particles and the applied external fields. For example, one of the most powerful and widely used are the optical tweezers, which uses a highly focused laser beam to generate a field gradient near the focus which generates a trapping force towards the focus. In the case of electric tweezers, the difference of dielectric properties between particle and surrounding medium determines the particle location. When a time-averaged induced dipole-field is generated on the particles due to an external field, if the particles are more polarizable than the surrounding medium, the particles will locate at the field maxima; however, if the medium is more polarizable, the particle will be trapped at the field minima. [4]

Currently, there is a lot of interest on using these methods to control and assembly particles with different shapes, including patchy, [25] ellipsoidal, [26] rod-like [4] and spherical particles. [27] Uniform spherical particles are the most widely used and studied geometry since the orientational change could be ignored in polarizable materials. As described above, researchers have more interest on tri-axial particles, such as rod-like particles, because of their directional dependence generated by the external field, which can promote more complicated assembled structures.

Experimental results show that particles generally align their long axis with the applied external field,[28,29] which is an intuitive result, generally understood as the induced dipole alignment with the field generates the minimum interaction energy. Whereas recently, experimental and analytical result both demonstrate the phenomenon that by simply change the external field conditions, both long axis and short axis of the particles could be aligned with the field. [30] [31] Such observations and theoretical models give a prediction that by varying particle geometry, different states could be achieved, for three-axial ellipsoidal particles, up to nine different orientations are possible. Generally, the electric field is recognized as the one that can provide good alignment on large number of particles but lack the ability to manipulate single particle compare with optical tweezers, which offer high resolution for trapping individual particles, although its limitation on large spatial control. [32] Precise control of anisotropic particles with electric field indicates that electric field can also generate high restriction on individual particle, however there is not estimation of the stiffness of the trapping. Future understanding of such phenomenon could be useful for particle control and directed assembly.

Direct measurement of the interaction of an anisotropic particle influenced by a non-uniform AC electric field play an important role on validating the theory and evaluating the control of particles position and orientation, which could improve the design and assembly of dielectric particles. The advance of particle assembly can lead to novel application in different areas, such as photonics, electronics, sensing and biomaterials.[33] One of the most powerful methods to measure the particle-field

interaction is to obtain the local energy landscape of a particle around the equilibrium state. By measuring the thermal sampling of a single particle, the probability distribution can be obtained and the potential energy landscape using the Boltzmann inversion is obtained. The potential energy landscape encloses information of forces, torques, and thermal sampling of the particle, which is a critical information to understand the control of anisotropic particles under the influence of non-uniform AC electric fields. Total Internal Reflection Microscopy (TIRM) is one of the new experimental techniques that can measure the distance between a single sphere particle and a substrate, the separation distance due to the contribution of the total interaction between them, the most probable distance is where the sum of the interactions is equal to zero, the most probable distance represents the minimum of the potential energy landscape between particle and substrate. Therefore, TIRM is a powerful technology to measure 1-D energy landscape of spherical particle. For 2-D energy landscape of colloidal particles with shape anisotropy, the inverted microscope is applied to capture video of a particle located around equilibrium position. The particle displacement and rotation are tracked, from where the 2-D energy landscape is calculated.

The energy landscape is characterized by the stiffness coefficient along the position and orientation, which determines the magnitude of the harmonic trapping well. The analysis of the stiffness relies on an approximation that when the particles are located at the potential harmonic well, the force field can be approximated with a linear form, which means that the harmonic potential has a quadratic form. By fitting

the energy to a quadratic function, the stiffness of the force can be obtained, and the similar concept can be applied on the analysis of the torques.[34]

In this work, we first measure the potential energy landscape of anisotropic particles under the influence of a non-uniform AC electric field, which is generated by different electrode configurations. The energy landscape of the anisotropic particle using parallel electrode has been studied in previous work, but the analysis of other type of electrodes, such as quadrupole and octupole have not been reported. Furthermore, new electrode configurations are designed to improve and develop the control of anisotropic particles. Typical parallel electrodes provide control on two dimensions but has no effect along the direction of the field. Otherwise, quadrupole and octupole electrode can trap particle in the center, but the electric field frequency produces no control on the particle orientation. To combine the advantage of both type of electrode, a new electrode configuration is studied.

Furthermore, the measurement and calculation of force and torque are developed through theory to have better understanding of the position and orientation control of anisotropic particles.

In the final part of this study, we describe the stiffness of the electric harmonic trapping using both numerical and analytic approaches to compare with experimental results.

2. THEORY

2.1. Superellipsoidal particle

In this study, we use a particle geometry that is defined by the superellipsoid equation, given by[35]

$$\left(\left|x'/\,r_x\right|^r+\left|y'/\,r_y\right|^r\right)^{n/r}+\left|z'/\,r_z\right|^n=1 \tag{1}$$

where r_x , r_y and r_z are the principal semi-axes of the particle, *n* and *r* are the parameter that define the particle shape. We set the value of *n* and *r* >1 so that the particles will have convex shape. Values of *n* and *r* smaller than 1 generate convex shapes that are not of interest in the present analysis. In the current study, we fit the aspect ratio ($r_x : r_y : r_z$) and particle shape (*n*, *r*) used in the experiment with the Eq. (1).

2.2. Laboratory and particle coordinates

To analyze the interaction between particle and non-uniform AC electric field, we define two system of coordinates, one attached to the particle, and the other attached to the electrodes, as explained below. Consider a superellipsoidal particle near a planar surface between a parallel electrode, as depicted in **Figure 1**. x', y' and z' are the axes of the particle frame, which correspond with the principal semi-axes of the particle. x, y and z represent the axes of laboratory coordinates,

which is fixed and attached to the electrode configuration; the origin of the laboratory coordinates is located in the plane of the symmetry of the electrode gap. We use Euler angles (θ,φ,ψ) to define the relative orientation of the particle respect to the electrode. θ is the azimuthal angle, φ represents the polar angle, and ψ is the rotation angle around the z'-axis. x represents the particle position relative to the origin of the laboratory coordinates, z is the distance from the particle center to the planar surface, and h is the smallest separation distance between particle and surface.

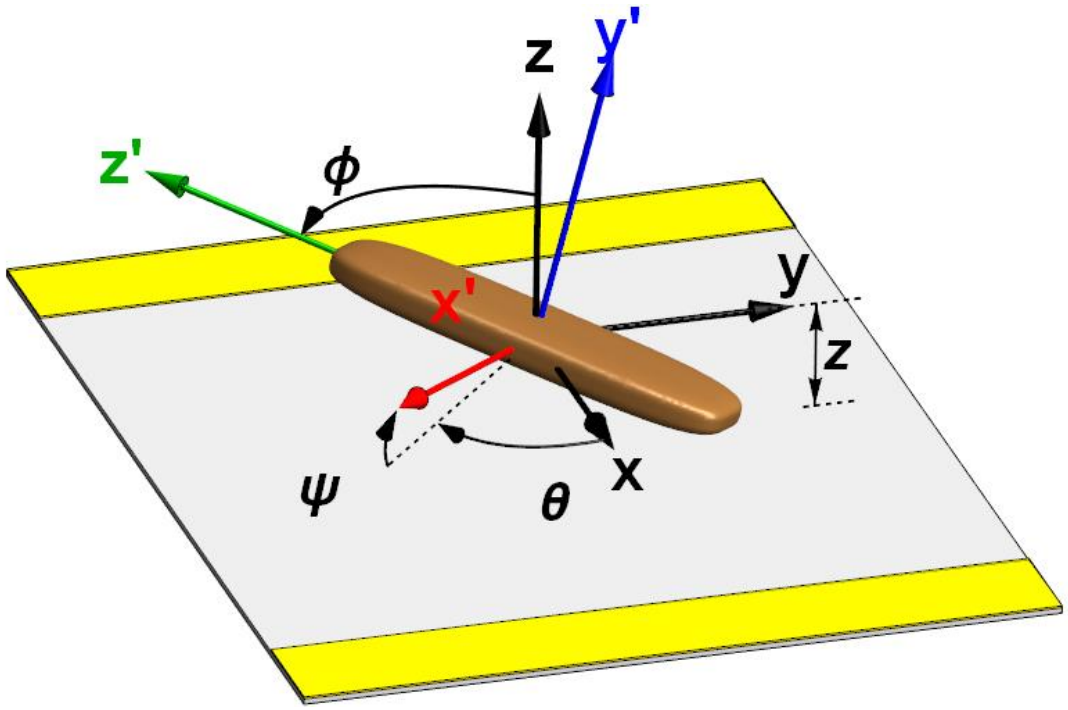

Figure 1. Schematic representation of a superellipsoidal particle with an arbitrary orientation between parallel electrodes. Primed axes (in color) represent the particle coordinates. Unprimed axes (in black) represent the laboratory coordinates. The particle orientation is characterized by the Euler angles (θ,ϕ,ψ). z denotes the particle position.

The variables in the laboratory and particle coordinates are correlated by the rotation transformation matrix, which is defined by [36] [37]

$$\mathbf{A} = \begin{pmatrix} A_{11} & A_{12} & A_{13} \\ A_{21} & A_{22} & A_{23} \\ A_{31} & A_{32} & A_{33} \end{pmatrix} = \begin{pmatrix} \cos\psi\cos\theta - \cos\varphi\sin\theta\sin\psi & \cos\psi\sin\theta + \cos\varphi\cos\theta\cos\psi & \sin\psi\sin\varphi \\ -\sin\psi\cos\theta - \cos\varphi\sin\theta\cos\psi & -\sin\psi\sin\theta + \cos\varphi\cos\theta\cos\psi & \cos\psi\sin\varphi \\ \sin\varphi\sin\theta & -\sin\varphi\cos\theta & \cos\varphi \end{pmatrix} \quad (2)$$

2.3. Net potential energy landscape

The net potential energy of a particle near a planar surface under the influence of an AC electric field takes into account the particle-wall potential and particle-field potential, such that

$$u^{net}(\mathbf{X},\Theta) = u^{pw}(\mathbf{X},\Theta) + u^{pf}(\mathbf{X},\Theta) \quad (3)$$

where $\mathbf{X} = (x, y, z)$ and $\Theta = (\theta, \varphi, \psi)$. In particular, we are interested on the interaction between a single particle and AC electric field in the gap between the electrodes; therefore, the particle-electrode interaction is not considered in the present analysis.

2.4. Particle-wall potential

The particle-wall potential prevents the particle, at different positions and orientations, overlapping with the substrate. Particle-wall interactions are the combination of two parts: electrostatic repulsion and van der Waals interaction. The repulsive force dominates the interaction while van der Waals potential can be seen as negligible for the separation between particles used in the present analysis. The net

interaction potential is given by[11,38,39]

$$u^{pw}(z,\theta,\varphi,\psi) = \frac{Z\exp(-\kappa h)}{\sqrt{\Gamma}} \tag{4}$$

$$Z = 64\pi\varepsilon_m(\frac{k_BT}{z_ve})^2\tanh(\frac{z_ve\psi_p}{4k_BT})\tanh(\frac{z_ve\psi_w}{4k_BT}) \tag{5}$$

where κ^{-1} is the Debye length, k_B is the Boltzmann's constant, T is the absolute temperature, ε_{m} is the dielectric constant of the medium, z_v is the electrolyte valence, e is the electron charge, ψ_{p} and ψ_w are the particle and wall surface potentials. Γ is the Gaussian curvature of the particle evaluated at the point with minimum separation distance between particle and substrate. h is given by [11]

$$h(z,\theta,\varphi,\psi) = z - S_{z,\min}, \tag{6}$$

where $S_{z,\min}$ is the distance from the particle's center to the surface's minimum along the perpendicular direction to the substrate, given by

$$S_{z,\min} = \left\{\left[\left|r_xA_{13}\right|^{\left(\frac{r}{r-1}\right)} + \left|r_yA_{23}\right|^{\left(\frac{r}{r-1}\right)}\right]^{\left(\frac{r-1}{r}\right)\left(\frac{n}{n-1}\right)} + \left|r_zA_{33}\right|^{\left(\frac{n}{n-1}\right)}\right\}^{\left(\frac{n-1}{n}\right)} \tag{7}$$

and the Gaussian curvature is defined by [11]

$$\begin{aligned}\Gamma = {} & \frac{S_{z,\min}^{\left(\frac{n+2}{n-1}\right)}(n-1)(r-1)}{r_x^2r_y^2r_z^2} \\ & \times\left[\left|r_xA_{13}\right|^{\left(\frac{r-2}{r-1}\right)}\left|r_yA_{23}\right|^{\left(\frac{r-2}{r-1}\right)}\left|r_zA_{33}\right|^{\left(\frac{n-2}{n-1}\right)}\right] \\ & \times\left[\left|r_xA_{13}\right|^{\left(\frac{r}{r-1}\right)} + \left|r_yA_{23}\right|^{\left(\frac{r}{r-1}\right)}\right]^{\left(\frac{2(n-r)}{r(n-1)}\right)}\end{aligned} \tag{8}$$

2.5. Particle-field potentials

The net particle-field potential encloses the gravitational potential and the induced dipole-field potential, given by superposition as

$$u^{pf}(\mathbf{X},\Theta) = u_g^{pf}(z) + u_{de}^{pf}(\mathbf{X},\Theta) \tag{9}$$

The gravitational potential energy relative to the surface is given by

$$u_g^{pf}(z) = v_p(\rho_p - \rho_m)gz \tag{10}$$

where v_p is the superellipsoid volume, ρ_p and ρ_m are the density of particle and medium, and g is the acceleration due to the gravity. For a particle shape $n = r = 4$ the volume is given by[40]

$$v_p = \frac{r_x r_y r_z}{2} \frac{\Gamma(1/4)\Gamma(1/4)}{\Gamma(1/2)} \frac{\Gamma(5/4)\Gamma(1/2)}{\Gamma(9/4)} = 6.482 r_x r_y r_z \tag{11}$$

where Γ is the complete gamma function (not the Gaussian curvature in Eq. (8)).

The potential energy between the induced dipole and the non-uniform electric field is[41]

$$u_{de}^{pf} = -k_B T \lambda \sum_{i=1}^{3} \left[\frac{f_{CM,i}}{|f_0|^2} (\mathrm{E}_i^{*\prime})^2 \right] \tag{12}$$

where $\lambda \equiv (3/4)(\varepsilon_m v_p / k_B T)|f_0|^2 (E_0^*)^2$ is a dimensionless parameter that represents the ratio between the magnitude of the applied electric field energy and the thermal energy. The index $i = 1,2,3$ (x', y', z') represents the principal axes of the particle coordinate, $f_{CM,i}$ represents the Clausius-Mossotti factor along the i-axis of the particle, f_0 is the Clausius-Mossotti factor of the shortest axis at zero frequency. The Clausius-Mossotti factor is defined by[41]

$$f_{CM,i} = \mathrm{Re}\left[\frac{1}{3}\frac{\tilde{\varepsilon}_{p,i} - \tilde{\varepsilon}_m}{\tilde{\varepsilon}_m + (\tilde{\varepsilon}_{p,i} - \tilde{\varepsilon}_m)L_i}\right] \tag{13}$$

Here, $\tilde{\varepsilon}_m$ is the complex medium permittivity, $\tilde{\varepsilon}_{p,i}$ is the complex particle permittivity along the *i*-axis of the particle. The complex permittivity is expressed as $\tilde{\varepsilon} = \varepsilon - i\sigma/\omega$, where ω is the electric field frequency, and σ is the conductivity. L_i is a parameter defined in the solution of Laplace's equation in ellipsoid coordinates, which quantifies the shape anisotropy of the particle along the i-axis[41]

$$L_i = \frac{r_x r_y r_z}{2}\int_0^\infty \frac{d\alpha}{\left(\alpha + r_i^2\right)\sqrt{\left(\alpha + r_x^2\right)\left(\alpha + r_y^2\right)\left(\alpha + r_z^2\right)}} \tag{14}$$

$E_i^{*\prime} = E_i'/(V_{pp}/\pi d_g)$ in the Eq. (12) is the normalized electric field along the *i*-axis of the particle, $V_{pp} = 2V_0$ is the peak-to-peak voltage, d_g is the electrode gap distance. E' is the electric field in the particle coordinates which is related to the electric field in laboratory coordinates by transformation matrix, as

$$\mathbf{E}' = \mathbf{A}\cdot\mathbf{E} \tag{15}$$

where the transformation matrix **A** is defined in the Eq. (2).

2.6. Electric field

The electric field, E, represents the electric field generated by the electrodes. The electric field between coplanar electrodes is[42]

$$\begin{aligned} E_x &= \frac{2V_0}{\pi d_g}\left[\tan^{-1}\left(\frac{\sin\hat{x}}{\sinh\hat{z}}\right) - \tan^{-1}\left(\frac{\cos\hat{x}}{\sinh\hat{z}}\right)\right] \\ E_z &= \frac{V_0}{\pi d_g}\left[\ln\left(\frac{\cosh\hat{z} + \cos\hat{x}\cosh\hat{z} + \sin\hat{x}}{\cosh\hat{z} - \cos\hat{x}\cosh\hat{z} - \sin\hat{x}}\right)\right] \end{aligned} \tag{16}$$

where, $\hat{x} = \pi(x+d)/2d + \pi/4$ and $\hat{z} = \pi z/2d$, d_g is the electrode gap.

The electric field generated by quadrupole and octupole electrodes is[43]

$$E_{quadrupole} = 8\frac{V_0}{d^2}R$$
$$E_{octupole} = 24\frac{V_0}{d^3}R^2 \quad (17)$$

where R is the radial distance from the quadrupole or octupole center.

2.7. Probability distributions & potentials

Boltzmann's equation is used to correlate the probability $p(\mathbf{X},\Theta) = p(x,y,z,\theta,\varphi,\psi)$ of the particle sampling different positions and orientations in infinite dilute conditions to the potential energy.

$$p(\mathbf{X},\Theta) = p(\mathbf{X}_r,\Theta_r)\exp[-(u^{net}(\mathbf{X},\Theta) - u^{net}(\mathbf{X}_r,\Theta_r))/k_BT] \quad (18)$$

where $u^{net}(\mathbf{X},\Theta)$ is the net potential energy introduced in Eq. (3), $\mathbf{X}_r$ and Θ_r are the reference position and orientation in the relative potential energy. Since the potential energy of the anisotropic particle is a function of six variables, it is necessary to reduce the dimensionality of the probability distribution and potential energy for visualization. The position-averaged probability distribution can be expressed as[44].

$$\langle p(\Theta)\rangle_{\mathbf{X}} = \frac{1}{(z_f - z_i)(y_f - y_i)(x_f - x_i)}\int_{z_i}^{z_f}\int_{y_i}^{y_f}\int_{x_i}^{x_f} p(x,y,z,\theta,\varphi,\psi)dxdydz \quad (19)$$

The limits of the integration of x and y are defined by the electrode's dimensions, z must greater than the longest particle axis. The position-averaged potential energy can be calculated through Boltzmann's relation as

$$\frac{\langle u^{net}(\Theta)\rangle_{\mathbf{X}} - \langle u^{net}(\Theta_r)\rangle_{\mathbf{X}}}{k_BT} = \ln\left[\langle p(\Theta_r)\rangle_{\mathbf{X}}/\langle p(\Theta)\rangle_{\mathbf{X}}\right] \quad (20)$$

Similarly, the angle-averaged probability distribution can be obtained as

$$\left\langle p(\mathbf{X})\right\rangle_{\Theta} = \int_{\psi_i}^{\psi_f}\int_{\varphi_i}^{\varphi_f}\int_{\theta_i}^{\theta_f} p(x,y,z,\theta,\varphi,\psi)\sin\varphi d\theta d\varphi d\psi \Big/ \int_{\psi_i}^{\psi_f}\int_{\varphi_i}^{\varphi_f}\int_{\theta_i}^{\theta_f}\sin\varphi d\theta d\varphi d\psi \tag{21}$$

The integration limits of angle are 0 and 180 degrees because of particle's orientational symmetry. The angle-averaged potential energy can be calculated as

$$\frac{\left\langle u^{net}(X)\right\rangle_{\Theta} - \left\langle u^{net}(\mathbf{X}_r)\right\rangle_{\Theta}}{k_B T} = \ln\left[\left\langle p(\mathbf{X}_r)\right\rangle_{\Theta} / \left\langle p(X)\right\rangle_{\Theta}\right] \tag{22}$$

2.8. Quasi-2D analysis

Another approach to get lower-dimensional probability distribution and energy landscape is the quasi-2D distribution of states projected onto a surface. This approach is often used in optical microscopy measurements[7,45,46]. The average probability relates to the position x and orientation angle θ of the particle is expressed as

$$\left\langle p(x,\theta)\right\rangle_{y,z,\varphi,\psi} = \frac{\int_{z_i}^{z_f}\int_{y_i}^{y_f}\int_{\varphi_i}^{\varphi_f}\int_{\psi_i}^{\psi_f} p(x,y,z,\theta,\varphi,\psi)dzdyd\varphi d\psi}{(z_f - z_i)(y_f - y_i)(\varphi_f - \varphi_i)\left(\psi_f - \psi_i\right)} \tag{23}$$

which can be used to calculate the projected potential $\left\langle u^{net}\left(x,\theta\right)\right\rangle_{y,z,\varphi,\psi}$ by

$$\frac{\left\langle u^{net}(x,\theta)\right\rangle_{y,z,\varphi,\psi} - \left\langle u^{net}(x_r,\theta_r)\right\rangle_{y,z,\varphi,\psi}}{k_B T} = \ln\left[\left\langle p(x_r,\theta_r)\right\rangle_{y,z,\varphi,\psi} / \left\langle p(x,\theta)\right\rangle_{y,z,\varphi,\psi}\right] \tag{24}$$

Previous analysis has shown that for a particle located in the middle of the electrode gap with a fixed orientation parallel to the *x*-component of the field, the net potential energy of the particle (eqn (2)) reduces to [47]

$$\frac{u^{net}\left(z\right)}{k_B T} = B_e \frac{\exp\left(-\kappa h\right)}{\sqrt{r_m^2 \Gamma}} + G\frac{z}{r_m} - 4\lambda \frac{f_{CM,i}}{\left|f_0\right|^2}\tan^{-1}\left(\frac{1}{\sqrt{2}}\operatorname{csch}\left(\frac{\pi z}{2d}\right)\right)^2 \tag{25}$$

where $G \equiv v_p\left(\rho_p - \rho_m\right) g r_m / k_B T$, $B_e \equiv Z r_m / k_B T$, and r_m is the semi-axis length of the particle. The minimum energy state gives the maximum ratio of the electrical and gravitational energy required for quasi-2D analysis as

$$\frac{\lambda}{G} = \frac{1}{4}\left|\frac{f_0^2}{f_{cm,i}}\right| \frac{\sqrt{2}}{\pi^2} \frac{d_g}{r_m} \frac{d_g}{d_g - 2z} \tag{26}$$

By inserting the definitions of λ and G, the ratio will be further simplified and yields the maximum applied voltage to consider a quasi-2D analysis is

$$V_{pp,\max} = \pi d_g \sqrt{\frac{\sqrt{2}}{\pi^2} \frac{\left(\rho_p - \rho_m\right) g}{3\varepsilon_m} \frac{d_g}{\left|f_{cm,i}\right|} \left(\frac{d_g}{d_g - 2z}\right)} \tag{27}$$

where in Eqs. (26)-(27) the analytical form is simplified via the following approximation

$$\frac{d}{dz}\left[\tan^{-1}\left(\frac{1}{\sqrt{2}}\operatorname{csch}\left(\frac{\pi z}{2d_g}\right)\right)^2\right] \approx \frac{\pi^2}{\sqrt{2} d_g}\left(1 - \frac{2z}{d_g}\right) \tag{28}$$

2.9. Force and torque on the particle

The polarization of an anisotropic particle is proportional to the electric field, such that

$$p = v_p\left(\varepsilon_p - \varepsilon_m\right) \cdot E^- \tag{29}$$

where E^- is the electric field inside the particle. The internal electric field along i axis is given by

$$E_i^- = \frac{\tilde{\varepsilon}_m}{\tilde{\varepsilon}_m + (\tilde{\varepsilon}_{p,i} - \tilde{\varepsilon}_m) L_i} E_{0,i} \tag{30}$$

The force on the particle generated by the interaction of the induced dipole and applied electric field is given by[48]

$$\mathbf{F} = (\mathbf{p} \cdot \nabla)\mathbf{E} = 3\varepsilon_{\mathrm{m}} v_p \mathbf{f_{cm}} (\mathbf{E} \cdot \nabla \mathbf{E}) \tag{31}$$

The torque generated by the misalignment of the induced dipole and the applied electric field can be calculated by[49]

$$\mathbf{T} = \mathbf{p} \times \mathbf{E} = 3\varepsilon_m v_p (\mathbf{f_{cm}} \mathbf{E}) \times \mathbf{E}\,. \tag{32}$$

2.10.Stiffness in one-dimension

To introduce the expression of the stiffness, we start by considering the Taylor series of the time-averaged force that is applied on the particle

$$F = F_{x=x_0} + \frac{dF}{dx}(x - x_0) + \ldots \approx F_{x=x_0} + \frac{dF}{dx}(x - x_0) \tag{33}$$

where x_0 is the equilibrium position of the particle. Based on the definition and the approximation that was introduced in the previous chapter (Eq. (31)), we take the first two terms of the Taylor series ($F_{x=x_0}=0$) and get the expression of the stiffness of position as

$$k_x = \left|\frac{dF}{dx}\right|_{x=x_0} \tag{34}$$

Since $F = -\frac{dU}{dx}$, the stiffness can also be expressed as

$$k_x = \left|\frac{dF}{dx}\right|_{x=x_0} = \left|\frac{d^2U}{dx^2}\right|_{x=x_0} \tag{35}$$

Similarly, taking the first two terms of the Taylor expansion respect to the angle θ, the expression of the stiffness of orientation as

$$\kappa_\theta = \left|\frac{d^2U}{d\theta^2}\right|_{\theta=\theta_0} \tag{36}$$

where θ_0 is the equilibrium orientation of the particle.

2.11.Stiffness in two-dimension

The force field in two-dimension can be expanded in a Taylor series around equilibrium position as

$$\mathbf{F}(\mathbf{X}-\mathbf{X}_0)=\mathbf{F}(\mathbf{X}_0)+\mathbf{J}_0\cdot\mathbf{X}+o(\mathbf{X}) \tag{37}$$

where $\mathbf{X}_0$ is the equilibrium position so that $\mathbf{F}(\mathbf{X}_0)=0$, and $\mathbf{J}_0=\mathbf{J}(\mathbf{X}_0)$ is the Jacobian evaluated at $\mathbf{X}_0$. Pérez García *et al.* [34] give a method to estimate the stiffness in two or higher dimension as

$$\frac{1}{2}\left(\mathbf{J}_0+\mathbf{J}_0^T\right)=\mathbf{A}\begin{bmatrix}-k_1^* & 0\\ 0 & -k_2^*\end{bmatrix}\mathbf{A}^{-1} \tag{38}$$

where k_1^* and k_2^* are the stiffness of position along the particle coordinates.

3. METHODS

The procedure of preparing the experiment in the inverted microscope is introduced in this chapter, including the micro-fabrication of superellipsoidal particles, fabrication of electrodes, chemical preparation of electrode cell, microscopy and image analysis. Additionally, we include synthesis procedure of fluorescent particles at the end of the chapter that can be used on future experiments.

3.1. SU-8 introduction

The material that we use to synthesize the particle is the SU-8, a widely applied negative epoxy-based photoresist. Initially, the SU-8 was introduced as thick-film resist, it was used to pattern the molds for the electroplating or microstructure. [50] But soon the SU-8 also became a very good material as thin-film resist and can be applied in other area of microfabrication, such as microfluidics. [50] SU-8 has a great importance because of its low absorption coefficient at wavelengths above 300 nm. SU-8 can form films with thickness in the millimeter range with aspect ratio up to 20 in a single step of photolithography process. Other factors, such as biocompatibility and structural stability also make SU-8 one of the most popular employed photoresist in microfabrication.[50]

3.2. Particle micro-fabrication

Particles with superellipsoidal shape were fabricated using photolithography technique. A silicon wafer is prepared and cleaned as the substrate before the experiment by rinsing it with acetone (Fisher chemical) and isopropanol (IPA) (Fisher chemical) and baked at 200 ºC to remove the agent. Then, the wafer is placed in the O_2 plasma etcher at 0.35 Torr and 100 W for 5 min for a complete cleaning. In order to release the particles from the wafer without sacrificing the integrity of the complex microparticle architecture, a sacrificial layer must be coated on the wafer before fabrication. Here, OmniCoat (MicroChem) was spin coated onto a silicon wafer as a sacrificial layer. Centering the wafer on the photoresist spinner and applying about 4 mL of OmniCoat on the center of the wafer, which diameter is 100 mm. If bubbles are introduced during the spin coating process, we use the dropper to remove them. Set the spin speed to 500 r.p.m. at an acceleration of 100 r.p.m.s^{-1} to spread the resist, followed by running at 3000 r.p.m. at an acceleration of 300 r.p.m.s^{-1} , and hold for 30 s. Heat the wafer at 200 ºC hot-plate for 1 min after coating, and cool down to room temperature. On the top of the OmniCoat layer, 4 ml SU-8 2002 (MicroChem) was applied and set the spin speed to 500 r.p.m. at an acceleration of 100 r.p.m.s^{-1} , and hold for 10 s; then increase to the final speed as 4000 r.p.m. at an acceleration of 300 r.p.m.s^{-1} , and hold for 60 s to achieve a 1 μm thick layer. The thickness of the SU-8 layer depends on the amount of solvent in the resist[50] and the final spin speed. The deposition of the resist layer is followed by a soft-bake to remove the solvent and harden the photoresist. We bake the wafer at 95 ºC for 4 min on the hot-plate; after

that allowing the wafer to cool to room temperature. The baking temperature and baking time is important. Longer baking time or high temperature will cause the resist film to crack or harden on the wafer surface. Additionally, shorter time or low temperature will make the layer unstable. The exact temperature and baking time depend on the resist property and layer thickness, the setting that applied in our experiments are decided through documents[51] and experience. A photomask (Photomask Portal) is used to pattern the particles. Place the photomask on the mask holder of the UV aligner (chrome side down). Put wafer into the aligner and press it close to the mask using hard-contact mode. The wafer is exposed under UV light with 50 mJ/cm^2. After exposure, the SU-8 that is exposed to UV light is cross-linked by baking the wafer on a 65 ºC hot-plate for 1 min, followed by 2 min on a 95 ºC hot-plate, and allowing the wafer to cool down to room temperature. The final step is immersing the wafer into SU-8 developer (MicroChem), gently shake the container to remove the unexposed SU-8. This process generally takes around 1 min, longer time is not recommended since the particle itself may be dissolved as well. Wafer is then rinsed with IPA and DI water, dried with nitrogen gas and placed in plastic box for upcoming experiments.

The microparticles are released from the wafer before the experiment by removing the sacrificial layer. To remove the OmniCoat layer, the wafer is immersed into PG remover (MicroChem) at room temperature for 10 min and use small brush gently lift off the microparticles from the substrate. Centrifuge and remove the excess PG remover, replace with IPA for at least 5 times, the particles are then rinsed with DI

water several times to remove IPA and finally dispersed in DI water. The DI water used for all the experiments was made from an in-home Milli-Q academic water purification system.

3.3. Surface modification of SU-8 microparticles

The SU-8 particle can be chemically modified before or after releasing from the wafer to render different properties. Normally, we produce hydrophilic particle on the substrate by immersing the wafer into 50%.vol sulfuric acid for 60 s and rinse with DI water immediately to remove the acid. During this process, the epoxy rings on the SU-8 molecule will be opened using acid-catalyzed reaction to provide hydroxyl groups on the particle surface.[52]

Generally, the hydrophilic SU-8 particle can keep stable in DI water for 2 days. To improve the stability of the particle, further modification is necessary. Here, we use tetraethyl orthosilicate (TEOS) (Acros organics) to generate a silica shell on the particle. Put the wafer in the glass plate, then add ammonium hydroxide (Fisher chemical) and ethanol (Fisher chemical) to make an 8.5% vol ammonia in ethanol solution. Calculate the amount of TEOS that enough to make the full solution 15 mM TEOS, separate the adding of TEOS into 4 steps separated by 1 hr. Strong agitation is necessary in order to avoid aggregation; and cover the plate to avoid evaporation. Once the coating finish, rinse the wafer with DI water to remove excess solution, and follow the procedure introduced above to lift off the particle from wafer.

3.4. Electrode microfabrication

3.4.1. Electrode patterning

The electrodes used in the experiment are designed in house and made by photolithography techniques. Glass slides to be patterned are cleaned by sonicating in IPA, acetone and IPA, for 30 min of each, and immersed in Nochromix (Godax laboratories) overnight, slides are totally rinsed with DI water before fabrication, finally drying with nitrogen. After cleaning, the slides are heated at 200 ºC on the hot-plate for 10 min to remove excess water that might remain on the slides. They are blown with nitrogen to remove any dust after letting them cool down to room temperature. Place the slides in the photoresist spinner, applying S1813, a positive photoresist, to and fully cover the surface of the slide. Ramp the spinner to 3000 r.p.m. at an acceleration of 150 r.p.m.s^{-1} for 60 s. then the slides are transported to hot-plate, heated at 95 ºC for 5 min to settle the photoresist.

Using the similar method to SU-8 particle fabrication, the slides after bake are set in the UV aligner to pattern the electrode structure with 80 mJ/cm^2. After exposure, the region that have been exposed can be washed off by immersing into CD-26 solution and gently shake until the geometry of electrode is clearly shown on the slide. It is then immediately rinsed with DI water to remove excess CD-26 to keep the pattern remains. The slides are finally dried by nitrogen. If the pattern is unperfect, S1813 can be removed by immersing the slides into acetone and fully clean the slide

before pattern them again.

3.4.2. Metal deposition

Deposition of metal is done in the Sharon vacuum e-beam evaporator. The process begins bringing the chamber to ambient lab pressure. Remove the slide holder after the door can be opened and load the slides around the outside of the holder, held in place by paper clips, make sure that the clips are not placed over the electrode pattern. Place sufficient excess metal in the crucible before close the door, e-beam will hit the metal to evaporate and cover the electrodes.

Once finish loading the slides, seal the chamber and pump down the pressure to 3×10^{-6} torr. The chamber must be kept at a sufficiently low pressure to avoid the oxidation of the evaporated metal. Load the procedure for metal deposition right after the desire pressure in the chamber is reached. For Au electrodes, applied Cr at 0.05 nm/s to form a 15 nm layer, and deposit a 30 nm Au layer at 0.05 nm/s.

Once the chamber is at the right pressure, start the cooling water and start the power of e-beam to heat the metal. Cover the crucible before reach the desire deposition speed to prevent impurity in the Cr metal deposit onto the electrode. Plug in the sample holder to begin rotating the holder which gives a more uniform deposition and remove the cover to start the deposition of Cr. After the process is finished, wait 2 min to let the Cr crucible cool down and then change to Au crucible, follow the similar procedure to deposit Au. Once the Au is done, cool down the crucible, ramp down the power of e-beam, vent the chamber and remove the sample

and Au crucible. The chamber needs to be vented again to protect the pressure sensor.

After deposition, place the slides in a staining jar and fill with acetone. Sonicate the slides until excess of Au is removed and the patterned electrode is clearly visible. Clean the slides as normal and check the electrode gap under microscope to make sure there is no connection between in the electrode gap. Finally, bake the electrode on 120 ^{o}C hot-plate for 15 min to reinforce the Cr and Au layer.

3.5. Experimental cell preparation

In most of our experiments, the particles are dispersed in water. Here, we describe the procedure to prepare the colloidal suspension for the experiment. Place a Viton® O-ring with 5 mm in diameter onto the electrode after it was mixed around in the high vacuum grease to seal the O-ring. Then, a drop of particle solution was placed inside the O-ring, a microscope cover slip was gently stick on the O-ring to prevent the evaporation. The last step before the experiment is to attach wires to the electrode. Normally, we use conductive carbon tape that produces the least damage to the electrode. A small piece of the carbon tape is cut. Scrape off the paint at the wire end, place the end of wire onto the leads of the electrode and the tape is placed atop. The other side of wires are connected to a function generator to provide AC electric signal for the experiment.

3.6. Microscopy techniques

3.6.1. Inverted microscope

Most of the experiments are done using an Axio Observer A1 inverted optical microscope (Zeiss) with a $63\times$ objective. Lenses for $1.25\times$ and $1.6\times$ zoom are also used sometime. The formula to calculate the pixel size for videos taken by the CCD camera (HAMAMATSU) that is attached to the microscope is:

$$\text{pixel size} = 1214\left(\frac{40}{\text{objective mag}}\right)\left(\frac{\text{binning}}{8}\right)\left(\frac{1}{\text{magnification}}\right) \tag{39}$$

We use an image grabber software Steampix to capture the video frames and then track the position and orientation of the particle in the video by a MATLAB code. The recording rate is determined by the nature of the experiment. The original recording rate is 28 fps, but to analyze the energy landscape, video should be captured for a long time to reach more possible positions and orientations. Also consider the size and the medium viscosity, which makes the particle move relatively slow, so faster frame rate will take the frames in which the particles did not move much from the previous equilibrium configuration. Summing up all the facts mentioned above, we generally use a rate of 5 fps in most of our experiments. Other parameters like the brightness and contrast can be adjusted as well to improve the performance of the experiment. By changing the brightness and contrast to make the particle become bright and darken the background area will remarkably improve the accuracy of the tracking calculation. The balance of the optical table is also an important factor that must be considered before every experiment. The table should be extremely flat to eliminate

the effect of gravity by adjusting the pressure of the valve under the table.

3.6.2. Confocal microscope

Confocal scanning laser microscopy (CSLM) experiments are conducted using a Zeiss LMS 5 scanner attached to an Axio 200M inverted microscope. The objective that applied in experiments include Zeiss $64\times$ objective and a Zeiss $100\times$ oil immersion objective. 488 nm line and 514 nm line on a 25-mW Argon ion laser are used as excitation source. Scanned images are taken in fast scan mode at 512×512 pixels with pixel size as 0.2 micron. Total scan time of one image is approximate 15.79 s. By adjusting the intensity of laser, pinhole size and other parameters to maximize the image quality. Vertical information of particle is collected by using Z-stack mode to take images at different elevation. Posterior analysis these images produce a 3D model of the fluorescent particle through a MATLAB code.

3.7. Synthesis of fluorescent SU-8 anisotropic particle

Fluorescent SU-8 particles used in CSLM experiments are synthesized by mix the fluorescent dye with SU-8 solution and follow the previous procedure to produce particles. 1.5 mg Rhodamine 6G (Aldrich chemical) are dissolved in 15 mL SU-8 2002 solution. Let the undissolved dye settle down overnight, then centrifuge the solution at top to further remove undissolved dye. This step will remarkably improve the uniformity of the SU-8 particles. Follow the particle synthesis process but increase the intensity of UV light to 70 mJ/cm^2.

4. RESULTS AND DISCUSSION

4.1. Particle shape and properties.

The superellipsoidal particles used in the experiments in the present analysis to measure the energy landscape of single particle under the influence of AC electric field are produced through micro-fabrication process with similar aspect ratio (r_x:r_y:r_z=2.5:1:10 μm). **Figure 2** shows an image of particles on the wafer after UV exposure with uniform shape.

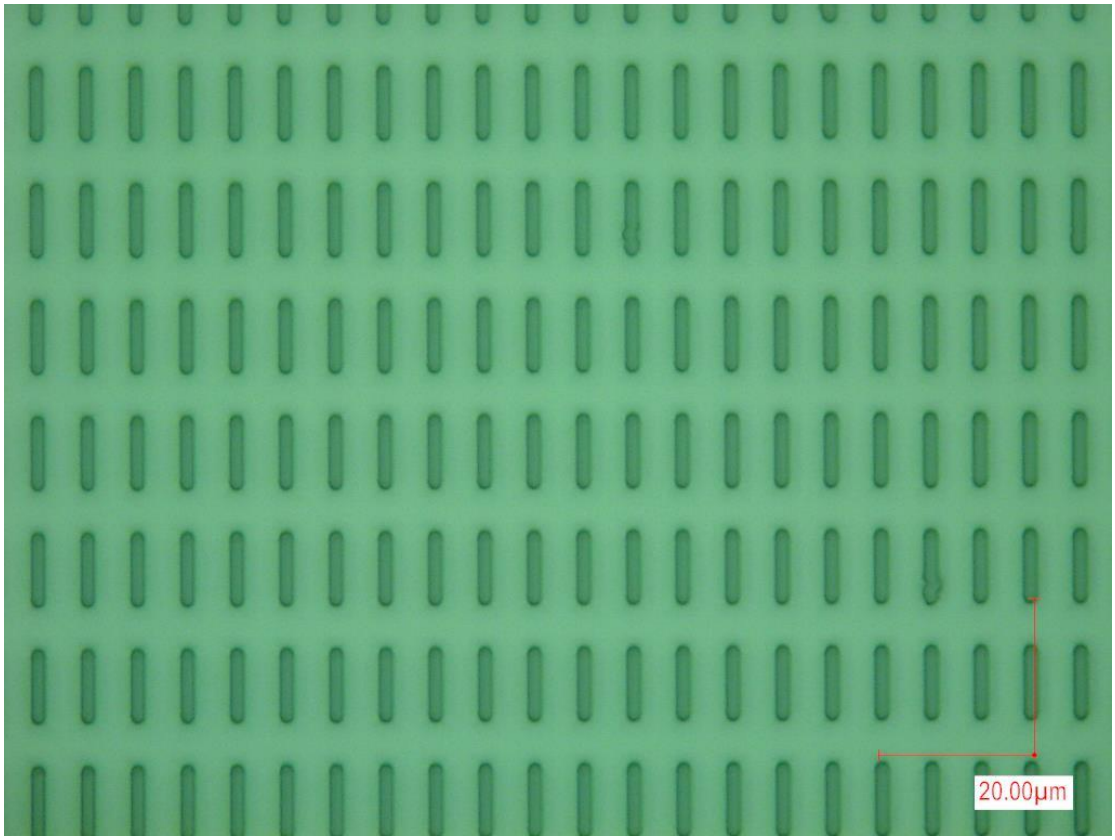

Figure 2. SU-8 superellipsoidal particles image under confocal microscope.

The parameters in **Table 1** describe the properties of particle and media used in simulation and theory calculations. The conductivities along the different axes are defined through previous experimental results. **Figure 3** shows the f_{CM} for a superellipsoidal particle as a function of AC field frequency. According to Eq. (13), the Clausius-Mossotti factor depends on the conductivity of each particle axis and the permittivity of particle and medium. These factors are identified through experiments and make the particle can reach at least four states by changing frequency. The particle state as a function of field frequency depends on the highest f_{CM} of the particle axis. At 0.1 MHz, $f_{CM,z}$ has the positive highest value, so the particle stays at the edge of the electrode with the longest axis parallel to the electric field. Between 0.2 MHz to 0.5 MHz, $f_{CM,y}$ has the highest value, so the particle is located close to edge of the electrode, but the longest axis perpendicular to the electric field. When the electric field frequency is larger than 0.5 MHz, f_{CM} are negative, which means the medium is more polarize than the particle, so that the particle will go to the middle of the electrode gap.

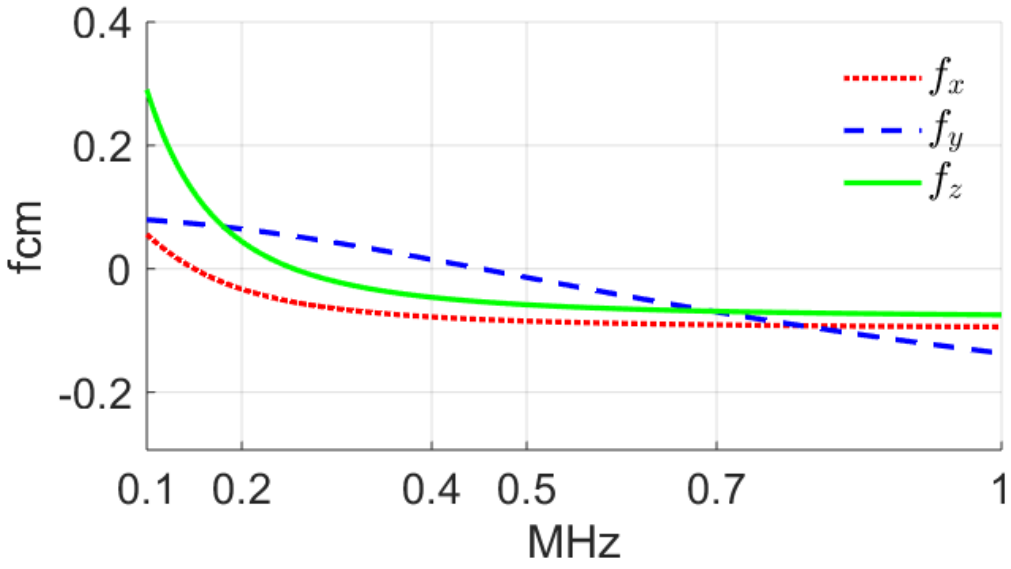

Figure 3. Clausius-Mossotti factors, f_{cm}, along the principal axis of particle vs. electric field frequency. f_x, f_y, f_z are Clausius-Mossotti factors along different particle axis.

Parameter	Value	Parameter	Value
ρ_p (kg/m^3)	1200	d_g (μm)	100
ρ_m (kg/m^3)	1000	$\varepsilon_p/\varepsilon_0$	3.2
κ^{-1} (nm)	33	$\varepsilon_m/\varepsilon_0$	78
Ψ_p=Ψ_m (mV)	-75	σ_m (μS/cm)	1

Table 1. Parameters used to calculate energy landscape.[4] ρ_p and ρ_m are the density of particle and medium material; κ^{-1} is the Debye length; Ψ_p and Ψ_m are the particle and wall surface potentials; σ_m is the conductivity of the medium; ε_m and ε_p are the dielectric constant of the medium and the particle; d_g is the dimension of electrode gap.

4.2. Particle probability distribution and potential energy

The experiments in this study are monitoring the equilibrium position and orientation of a single particle within AC field between different electrode configurations using an inverted microscope. **Figure 4** shows the result of tracking the position (x, y) and orientation (θ) of a single particle for about 60000 frames taken from the experimental video for 120 min. **Figure 4** (a) and (d) show the probability distribution and energy landscape of a single particle sampling around the equilibrium configuration between parallel electrodes. Here, x is the distance from particle center to the most probable position in x-direction. Between the parallel electrodes, due to the uniformity of the electric field along y-direction generated by the electrode symmetry, we did not consider a variation along y-direction. Due to the gravity and the electrostatic interaction between particle and substrate surface, particle stays stable close to the substrate, where the motion in z, ψ and φ directions are limited and not directly measured. **Figure 4** (b) and (e) show the probability distribution and energy landscape of a particle interacting with the electric field generated by a quadrupole. Similarly, **Figure 4** (c) and (f) shows the probability distribution and energy landscape for the octupole electrode configuration. When we analyze the quadrupole and octupole electrodes, we use r instead of x, which represents the distance from particle center to the most probable position.

Figure 4 (a) and (d) show that the particle orientation is confined in 5 degrees from the equilibrium configuration, and the particle position is confined within 10

microns from the equilibrium position. However, parallel electrode configuration does not confine the particle along the y-axis. These two figures show that parallel electrode provide powerful control on the orientation θ and position x of the particle. **Figure 4** (e) and (f) show that particle is restricted in the center of the electrode and it does not present any orientational dependence, which means that these configurations confined the particle position, but not its orientation.

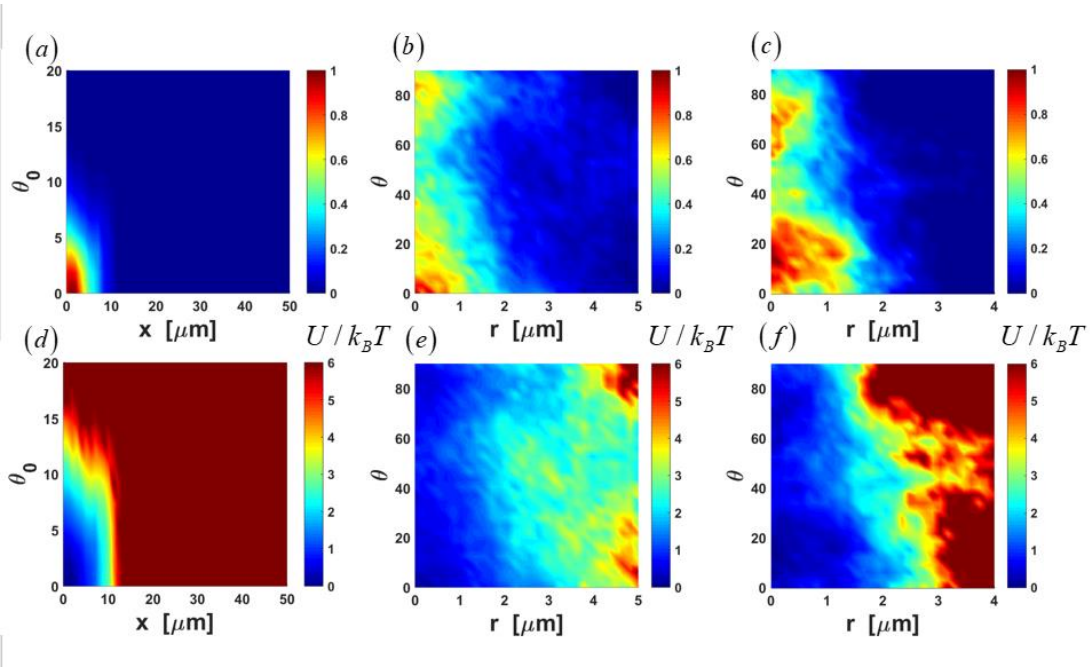

Figure 4. Normalized time-averaged particle probability distribution (a)-(c) and net potential energy landscape (d)-(f) as a function of position and orientation. x is the distance from particle center to the energy minimum. Figure (a) and (d) are results shown for parallel electrode experiment, here $\theta_0 = \pi - \theta$, (b) and (e) are results for the quadrupole electrode, (c) and (f) are results for the octupole electrode. The electric field condition for each experiment are 2 V_{pp}, 2 MHz.

Figure 5 shows the simulation results for the energy landscape of a particle under the influence of the electric field generated by a (a) quadrupole and (b) octupole electrodes with same electric field strength and frequency (2 V_{pp} and 2 MHz). The results in **Figure 5** show no orientational dependence. The results in **Figure 3** (e) and

(f) illustrate that the simulations match very well the experimental results. In **Figure 5** (b)-(c), it seems that 45 degree has the lowest probability compare with other orientations. This apparent minimum can be improved by capturing a longer video to get enough data reaching all the possible equilibrium orientations.

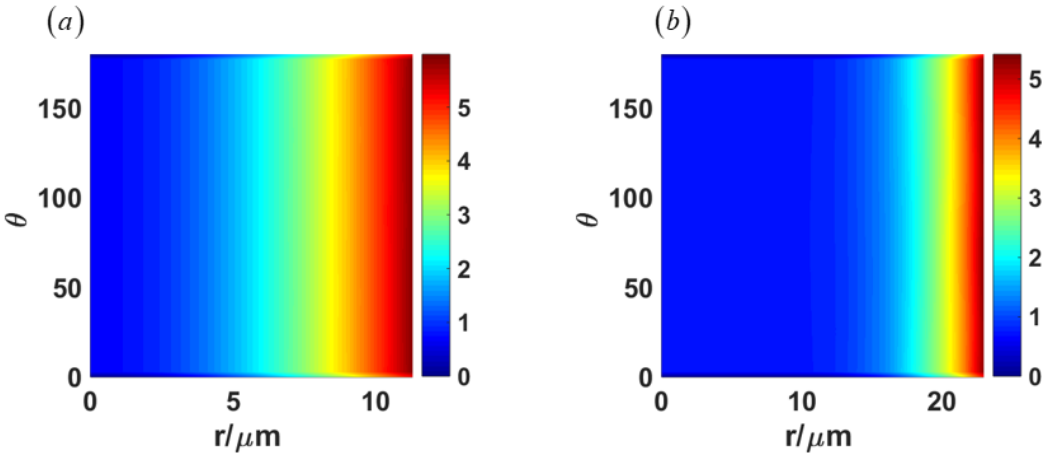

Figure 5. Simulation result of averaged potential energy landscape (*k*T units) as a function of the azimuthal angle θ and particle position *r* respect to the center of the (a) quadrupole and (b) octupole electrodes. The electric field conditions are same to the previous experiments (2 V_{pp}, 2 MHz).

4.3. Force and torque

We calculate the force and torque of the particle interacting with the AC electric field using Eqs. (31) and (32). Here, we limit our calculations to the force and torque applied on a superellipsoidal particle between parallel electrodes. Figure 6 shows the force along principal axes in laboratory coordinate between the electrode gap. The

origin is located in the middle of the electrode gap. Figure 6 (a)-(b) show the results under 0.1 MHz . The edge of electrode is at 50 and -50 μm, and the perpendicular dash line indicates the equilibrium position of particle when the particle is located at the edge of the electrode. At this point (45 μm), the force along x direction is approximately equal to zero, which separates the region on the left that pushes the particle towards the middle of the electrode gap, to the right that pushes the particle towards the edge. As we discussed before, the uniformity of the field on y direction produce no force on the particle. Force along z direction is shown in Figure 6 (b), F_z normally is balanced by the gravity and dielectric force between particle and the substrate. The maximum value of F_z appears between the equilibrium position and the edge, and it decreases dramatically from positive to negative. In the case of the field frequency equal to 1.0 MHz, the equilibrium position is at 0 μm, the force around equilibrium position will push the particle to the center which match the analysis of the energy landscape result. The maximum force appears close to the edge of the electrode, and the minimum absolute value of F_z is reached at the equilibrium position. In addition, the force is also affected by the orientation of the particle, in this analysis, we set the particle at the most probable orientation under the electric field conditions, which is obtained through energy landscape result.

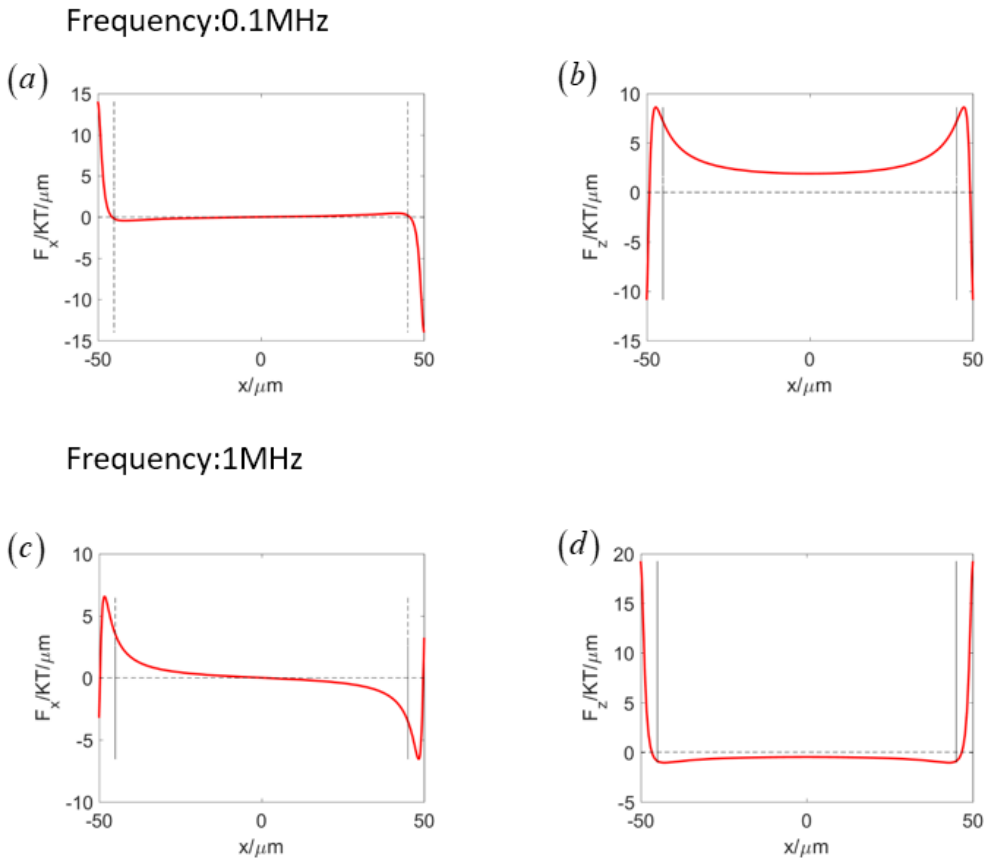

Figure 6. Particle field interaction force along x (F_x) and z (F_z) directions as a function of position x between parallel electrodes. x=0 is the middle of the electrode gap. AC field conditions are: (a) and (b) 0.1 MHz, 1 V_{pp}; (c) and (d) 0.1 MHz, 1 V_{pp}. The orientation of the particle is fixed in this analysis (θ=90°, φ=90°, ψ=0°)

In our research, we are more interested in the condition when particles are located around the equilibrium state. *i.e.* in the calculation of the force that restricts the particle movement in the middle of the electrode gap. From eqn (31), we know that the force is a function of position (x, y, z), orientation (θ, φ, ψ), and electric field conditions (ω, V_{pp}).

In **Figure 7**, the force around equilibrium position is plotted versus the applied peak-to-peak voltage V_{pp}. Since at the equilibrium position the force is zero, we use

the maximum force within 10 microns around equilibrium position. As shown in **Figure 7**, the force increases with voltage under both conditions.

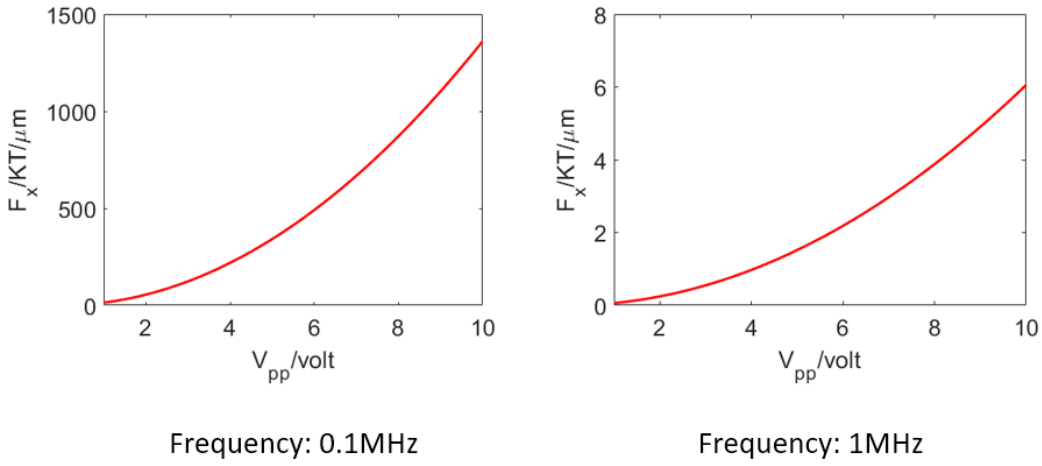

Figure 7. Particle field interaction force along x (F_x) and z (F_z) direction as a function of the peak-to-peak voltage (V_{pp}) between parallel electrodes. Field conditions: 0.1 MHz 1 V_{pp} (left); 1 MHz 1 V_{pp} (right). The particle is set at equilibrium position and orientation.

Figure 8 shows the force as a function of AC field frequency. Since the equilibrium position of the particle change with AC field frequency, the analyzed position is changing as the frequency increases. In the left figure, the dashed line represents the crossover frequency, for conditions with lower frequency, the force is calculated when the particle is located at x=50 μm, and at higher frequencies, the force is calculated when the particle is located at x=5 μm. It shows that when particle stays at the edge F_x decreases with frequency, and when particle locate in the middle of the electrode gap, the F_x is much lower than close to the edge. The figure on the right shows that F_z decrease with frequency at the edge, and it becomes close to zero in the middle of the electrode gap.

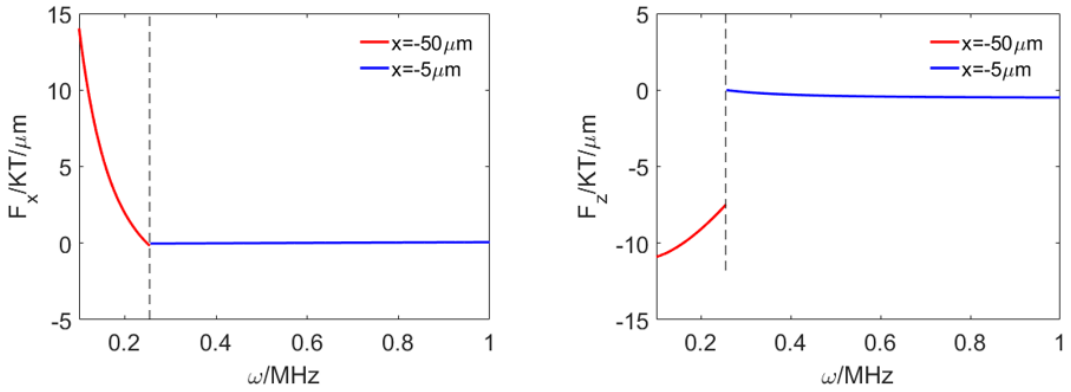

Figure 8. Force on a particle along the x (F_x) and z (F_z) direction as a function of the field frequency between parallel electrodes. The red line data stands for the data calculated when particle is located at the edge of the electrode; and the blue line is for the data calculated when particle locate close to the middle of the electrode. The dashed line represents the crossover frequency when the particle moves from edge to the middle of the electrode gap.

Figure 9 and **Figure 10** are calculated based on the statistic simulation results, and they show the energy landscape between parallel electrodes. The white arrows in the figures represent the orientation and magnitude of force in the x-direction F_x. These two figures show the tendency of the force match the simulation result of the energy landscape.

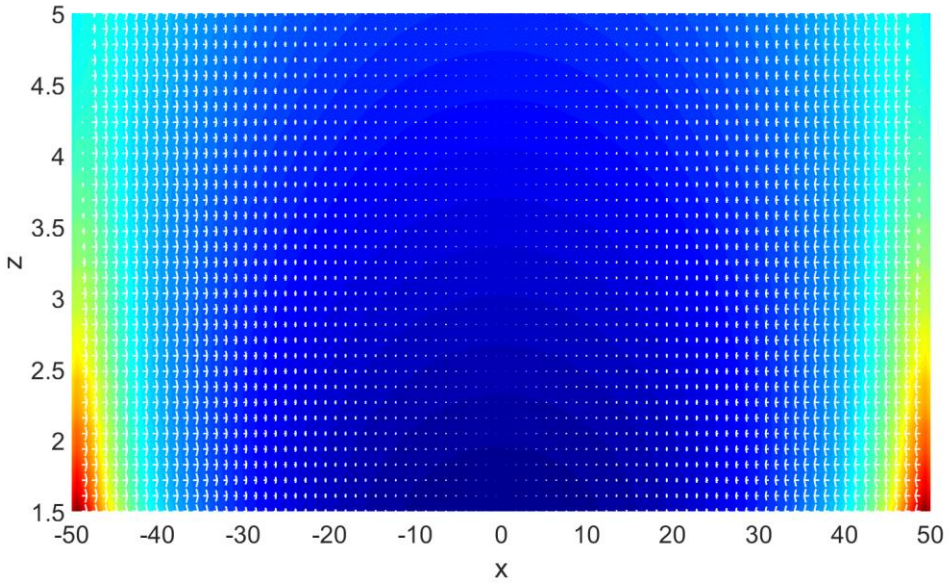

Figure 9. Energy landscape of single superellipsoidal particle between parallel electrode as a function of particle position (x, z). The arrows represent the force along the x-direction applied on the particle (1 MHz - $1V_{pp}$).

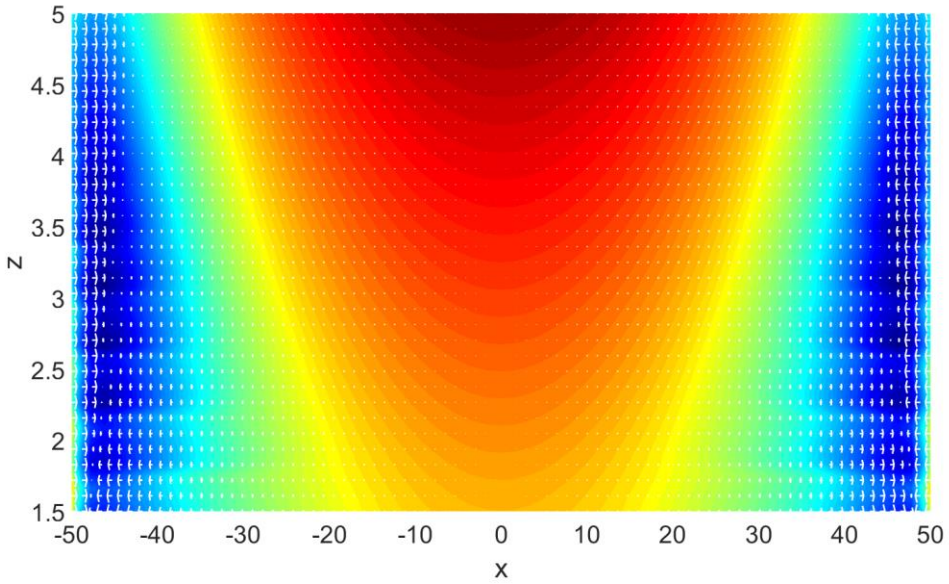

Figure 10. Energy landscape of single superellipsoidal particle between parallel electrode as a function of particle position (x, z). The arrows represent the force along the x-direction applied on the particle (0.1 MHz $1V_{pp}$).

A similar method is applied to analyze the torque applied on the particle. **Figure 11** shows the torque applying on the particle along the principal axes as a function of the azimuthal angle θ. As shown in Eq. (32), the torque is also a function of the

particle position, orientation, and AC field strength and frequency. In **Figure 11** (a), the AC field frequency is set to 1 MHz, so the position of particle is fixed in the middle of the electrode gap, and the applied voltage is 1 V_{pp}. We set angles other angles (φ, ψ) constant since the particle is mostly parallel to the surface. Torque along *z*-axis changes with azimuthal angle, and it reaches a maximum value when θ = 45° and 135°. The torque along the other axes are equal to zero under these conditions. In **Figure 11** (b), the AC field frequency equals to 0.1 MHz, the electric field generates a torque on to all three axes. It is shown that the applied torque along the *x* and *y* directions are much higher than T_z. Compare (a) and (b), T_z has the same tendency under different frequency.

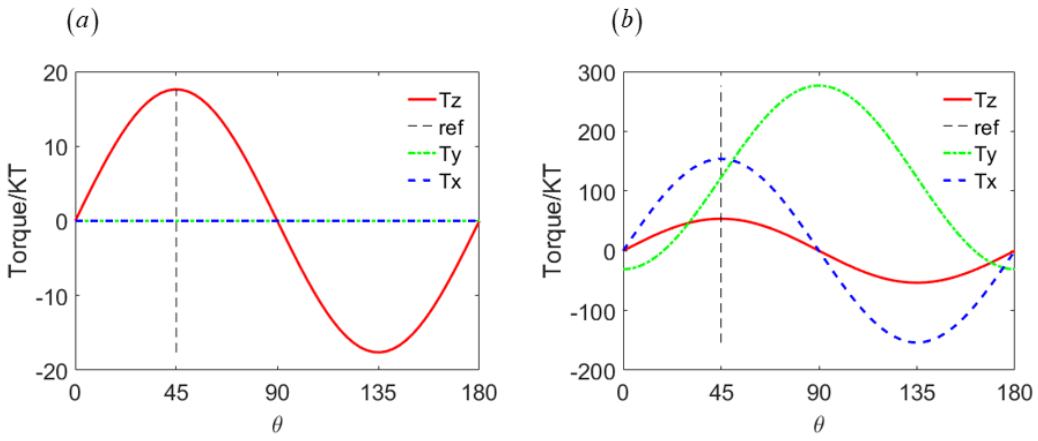

Figure 11. Torque along each axis as a function of the azimuthal angle θ. Field conditions (parallel electrodes): (a) 1 MHz 1V_{pp}; (b) 0.1 MHz 1V_{pp}. Particle configuration: θ=90°, φ=90°, ψ=0°. In (a), particle stays in the middle of the electrode gap. In (b), the particle stays at the edge of the electrode.

In **Figure 12**, the maximum torque along every axis are plotted as a function of applied voltage. In the left figure, the particle position is set in the middle of the

electrode gap, and for the right figure the particle is set close to the edge of the electrode. The torque along the x and y axes are approximately equal to zero when particle in the middle of the gap, and T_z increases with as the peak-to-peak voltage increases.

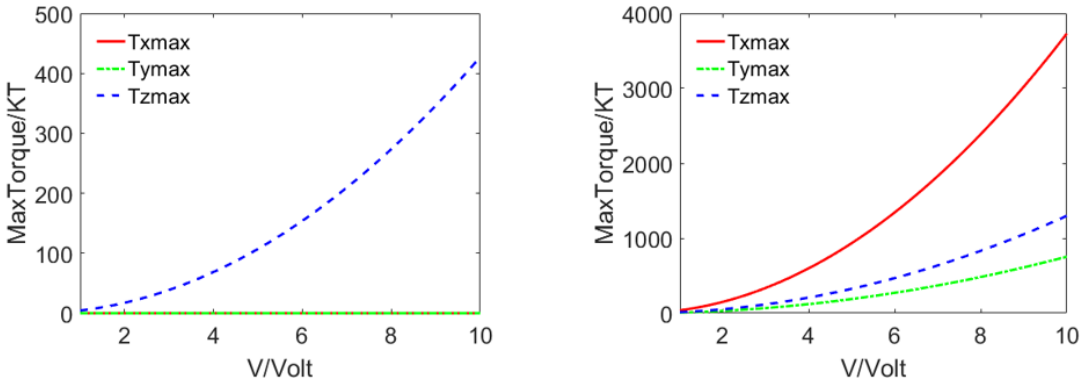

Figure 12. Maximum torque along each axis as a function of the peak-to-peak voltage. Field conditions (parallel electrodes): (a) 1 MHz - 1 V_{pp}; (b) 0.1 MHz - 1 V_{pp}. Particle configuration: θ=90°, φ=90°, ψ=0°. In (a), particle stays in the middle of the electrode gap. In (b), the particle stays at the edge of the electrode.

Figure 13 shows the maximum torque as a function of the AC field frequency. The left figure corresponds to the particle located in the middle of the electrode gap. The right figure corresponds to the particle located at the edge of the electrode gap. It is seen that the maximum torque along the z-axis $T_{z,\max}$ decreases with frequency, as shown in the left panel of **Figure 13**. Additionally, in the right panel that corresponds to a particle located at the edge of the electrode gap, it is shown that $T_{y\max}$ reaches a maximum value at about 0.3 MHz, and the sign of the torque is inverted at high frequencies.

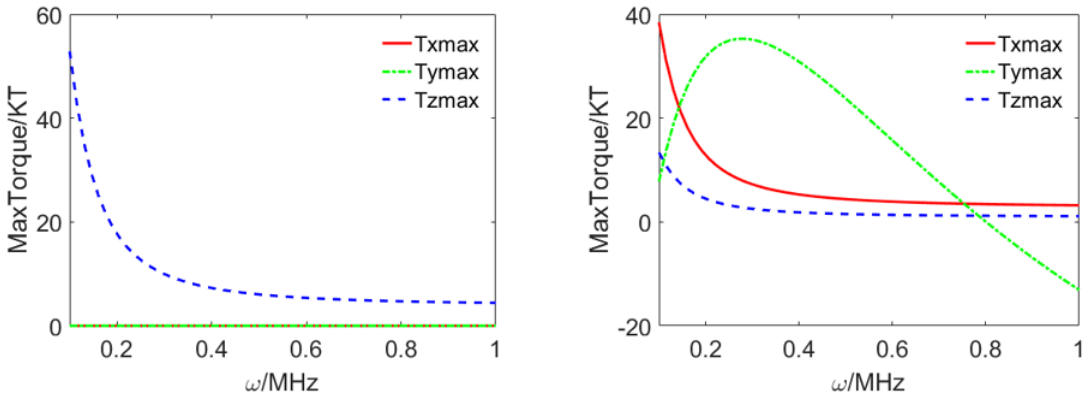

Figure 13. Maximum torque along each axis as a function of the field frequency. Field conditions (parallel electrodes): (a) 1 MHz - 1 V_{pp}; (b) 0.1 MHz - 1 V_{pp}. Particle configuration: θ=90º, φ=90º, ψ=0º. In (a), particle stays in the middle of the electrode gap. In (b), the particle stays at the edge of the electrode.

Figure 14 shows the correlation between torque and energy. The potential energy is averaged by polar angle and azimuthal angle, the white arrows represent the orientation and absolute value of the torque. The torque along the *z*-axis depends on θ, while T_y corresponds to a rotation around the polar angle. The white arrows represent the torque direction, which are pointing towards the minimum equilibrium state under these conditions (1 MHz – 1 V_{pp}).

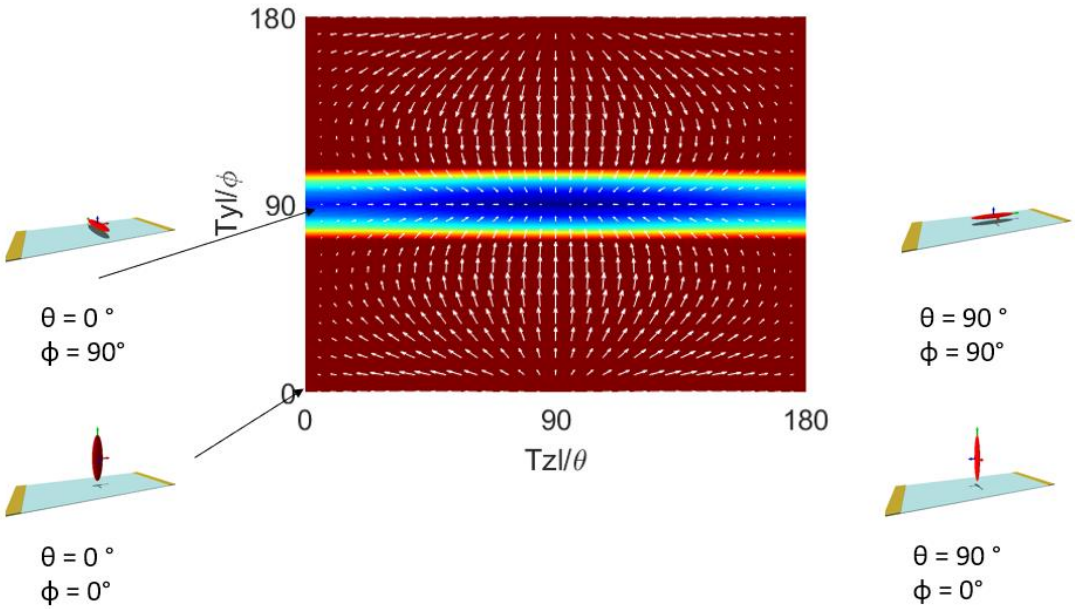

Figure 14. Orientation averaged potential energy landscape as a function of the azimuthal angle θ and polar angle φ. The particle is located between the parallel electrodes. Field conditions: 1 MHz - 1 V_{pp}. The arrows represent the torque vector generated by the energy land scape.

In this chapter, we described the analysis and quantification of the force and torque applied on a superellipsoidal particle under different field conditions generated by parallel electrode configuration. The results are useful to describe the dynamic behavior of a single anisotropic particle under the influence of an AC electric field. Furthermore, the force and torque directions over the averaged position and orientation energy landscapes show the accuracy of the present result for particles in AC electric fields.

4.4. Stiffness

In this section, we introduce the result of the stiffness calculation based on the definition and theory, which has been introduced in Chapter 2. **Figure 15** shows the

1-D averaged energy landscape as a function of (left) position x and (right) orientation θ. It is seen that around equilibrium position and orientation the averaged potential energy is approximately a quadratic function of x and θ, which corresponds to the basic assumption in the analysis of stiffness.

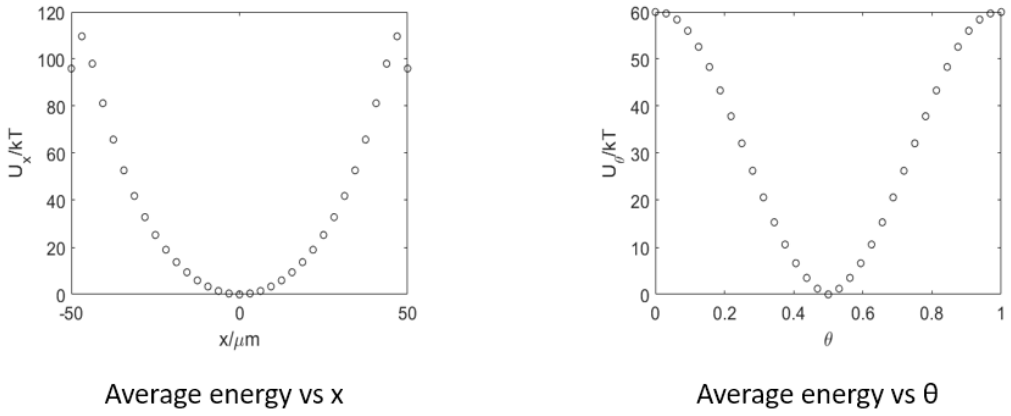

Figure 15. Averaged potential energy landscape as a function of (left) position x and (right) orientation θ/π. x=0 corresponds to the center of the electrode gap (gap size d_g=100 microns).

In this research, we introduce two approximation methods to calculate stiffness of single particle between parallel electrodes. The first is the analytical method, which uses the Eqs. (35) and (36). The stiffness for position and orientation can be obtained individually. The other method uses the quasi-2D potential energy landscape that was calculated in a previous analysis, which is averaged to a one-dimension energy landscape. Further, we fit the energy landscape around the equilibrium position with quadratic function of position x and orientation θ. The result of the stiffness is given through the definition of Eqs. (35)-(36).

Figure 16 shows the results for the stiffness using the two approaches described above, and the comparison with the experimental data. In both panels, data is plotted in logarithmic form, so the intercept of the linear fit is the value of the stiffness. Figure 16(a) shows that the two methods fit perfectly with the experimental results. **Figure 16** (b) shows that the numerical method, which considers the six-dimensional energy landscape, matches very well the experiments; however, the analytical method, which considers the cross section of the energy landscape, underestimates the magnitude of the stiffness. The reason of the difference is attributed to the fact that the analytical method considers the cross section (x,θ) of the potential energy landscape, while the other variables are kept constant.

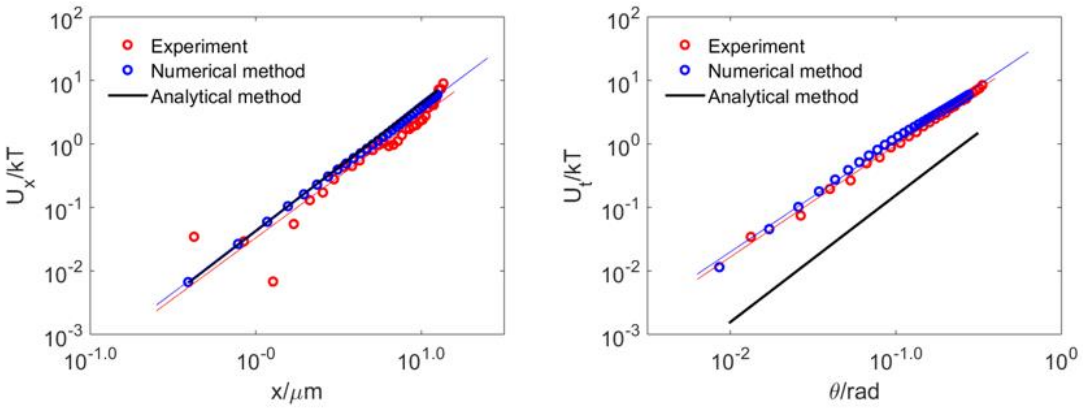

Figure 16. The comparation between experiments and two approaches to calculate the stiffness. The red markers correspond to the experimental data, blue markers correspond averaged of the six-dimensional energy landscape. Red and blue lines are fitting lines for the corresponding data points. Black line is calculated from Eqs. (34) and (36).

In **Figure 17**, the stiffness is plotted as a function of the AC field frequency and peak-to-peak voltage using the two aforementioned methods. **Figure 17** (a) shows the numerical method and **Figure 17** (b) shows the analytical method. In both cases, the

stiffness increases with the field strength. Furthermore, it is seen different regions as the frequency increases. The same effect is shown in **Figure 17** (b), the stiffness behavior is clearly separated at 0.2 MHz and 0.5 MHz, these two frequencies corresponds to crossover frequency regions, which has been mentioned in the analysis of Clausius-Mossotti factor in **Chapter 2**.

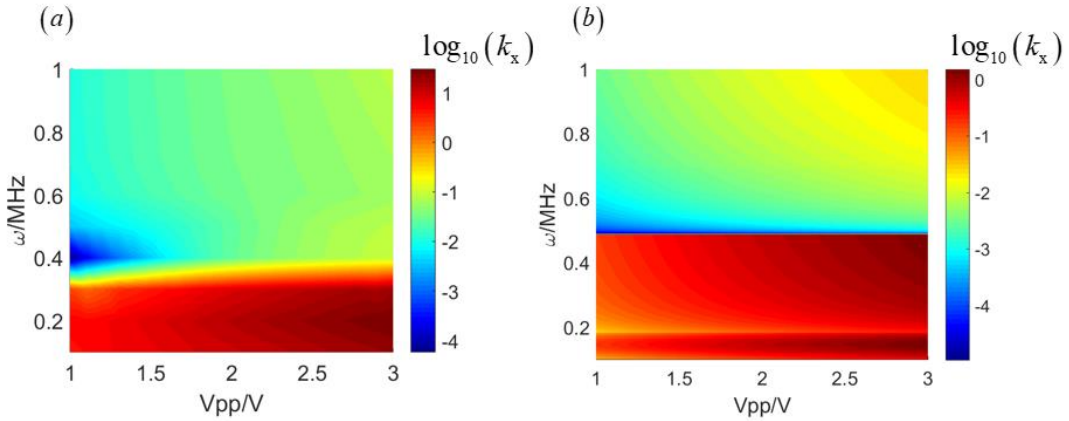

Figure 17. Stiffness of position (k_x) as a function of the AC voltage and frequency. The stiffness is calculated using the (a) average of the six-dimensional energy landscape, and (b) the analytical method.

To verify the relationship between stiffness of position and crossover frequency, the stiffness is plotted as a function of frequency at specific voltage and compare with **Figure 3**, as shown in **Figure 18**. The black dashed line shows that the crossover frequencies are correlated with the change in the stiffness magnitude.

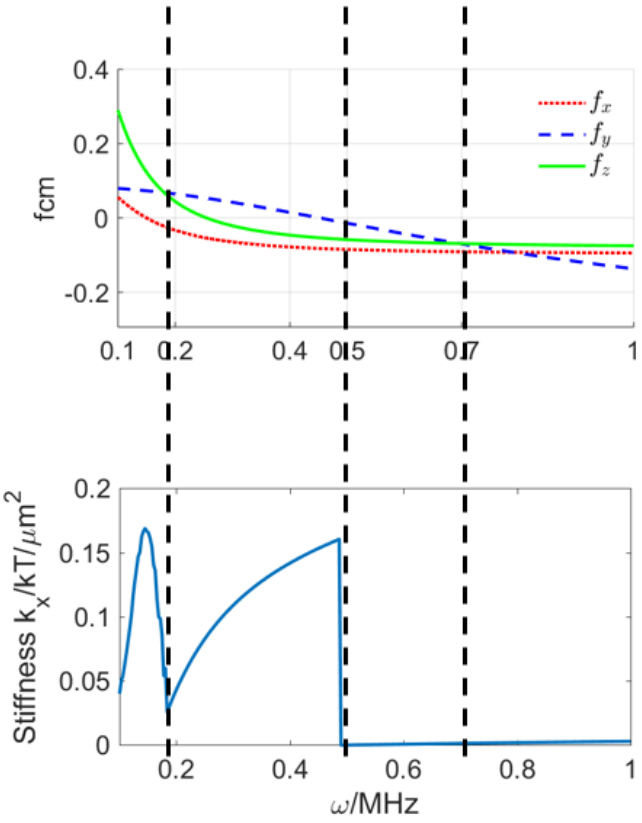

Figure 18. Relationship between the stiffness of position and the crossover frequencies. Black lines in the figure indicate the crossover frequencies. ω= 0.1820 MHz, particle stay close to the edge and becomes oriented perpendicular to the electric field. At ω= 0.5012 MHz, the particle stays in the middle and is perpendicularly oriented to the field. At ω= 0.7079 MHz, the particle is oriented parallel to the electric field and stays in the middle of the electrode gap.

Previous reports have introduced frequency dependent control of anisotropic particles using coplanar parallel electrode[4], but this kind of electrode has no affect along the *y*-direction, which is perpendicular to the electric field. On the other hand, quadrupole and octupole electrode which are widely used in particle assembly[53] can restrict dielectric particles in the center area but do not have the ability to generate frequency dependent orientational control of the particle. To combine the capabilities of these two kinds of electrodes, a new electrode configuration is designed through numerical simulations. The simulation process includes building the 3-D model of

electrode, the electric field calculation, and potential energy landscape calculation of new electrode configuration.

4.5. 3-D model of the new electrode

To build the new electrode configuration and calculate the electric field, we use COMSOL Multiphysics to simulation the electric field. We select 3D model in the COMSOL model wizard, applying electrostatic physics and Stationary study. Electrode model of this simulation can be seen in **Figure 19**. We set the length unit in micron. In **Figure 19**, the two cuboids represent the glass substrate of electrode separated by a gap with different geometry. Here, we define the ellipsoid gap which is the experimental region of interest, the semi-axis of ellipsoid is 200 microns and 50 microns, respectively. The two smaller electrode gaps are equal to 20 microns. We Set the cuboids much larger than gap to make the simulation close to reality condition. Finally, add a large block to enclose all the objects, which represent the external environment. After defining the geometry, the next step is to set the material properties. As described in the previous chapter, we use Au-Cr electrode, Cr layer is to stabilize the Au layer, and the thickness of both layers are both much smaller than substrate. So, in the simulation, we set the material of the upper surface of cuboids as gold to represents the electrode and ignore the thickness of the layer. In the experiment, particles are manipulated in aqueous system, so the large block in the

simulation is set as water. Final step before calculation is to define the electric potential value and boundary conditions. In the simulation, set V_{pp} value of electrode to 1 V and all the surface of environment block as ground surface to define the boundary condition. Under this setting, COMSOL Multiphysics can calculate the electric field, export the data above the electrode surface and follow the Eqs. (19)-(22), to calculate the energy landscape and the probability distribution, as shown in **Figure 20**.

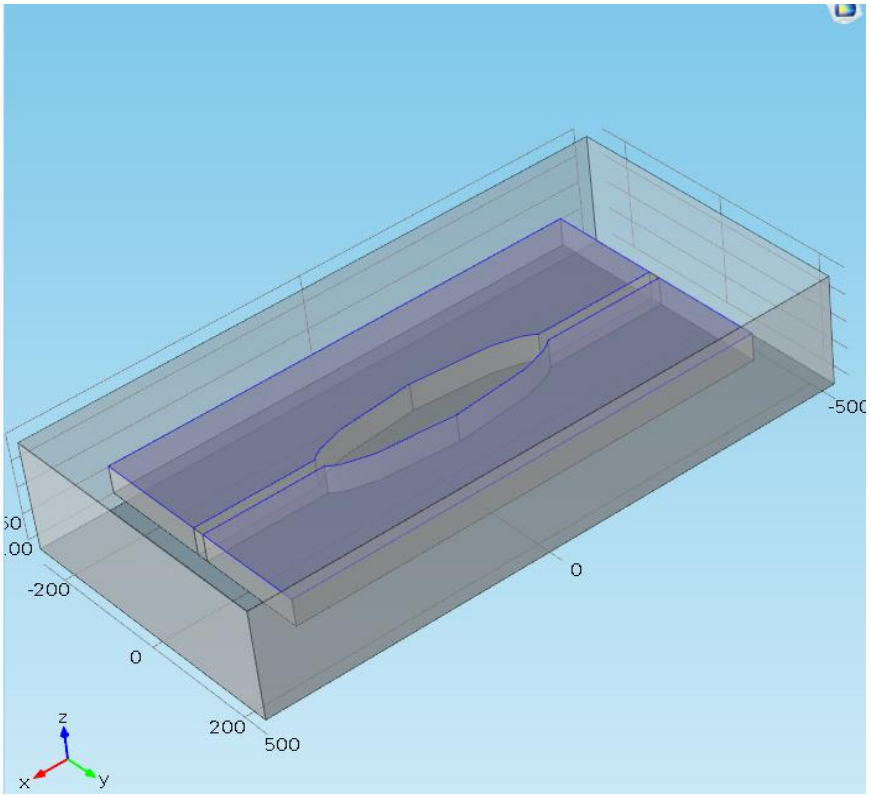

Figure 19. 3D simulation model of the electrode with elliptical shape using COMSOL. Dark part in the figure represents the gold layer coated on the silica substrate. The largest box represents the fluid medium (DI water).

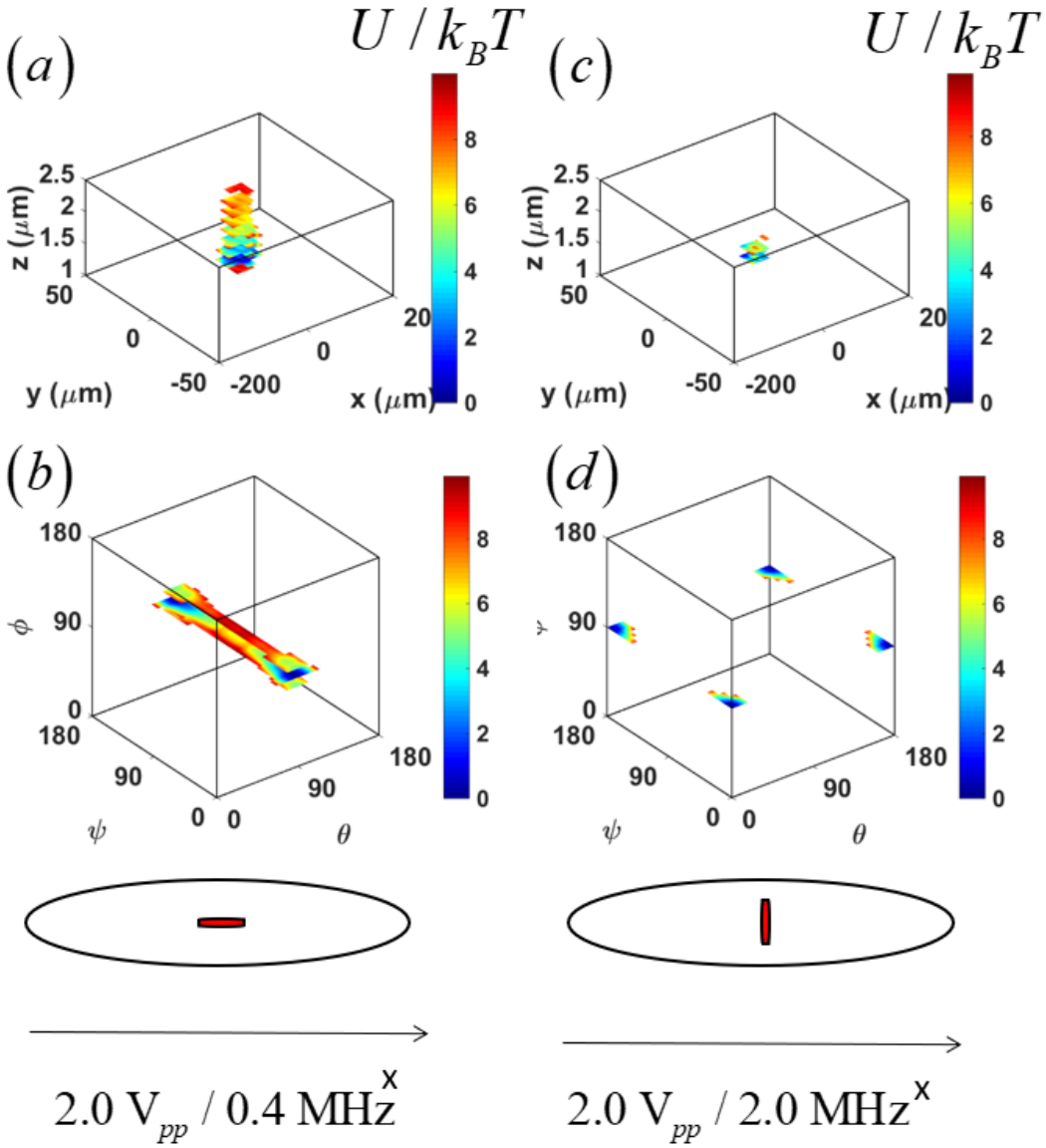

Figure 20. Position (a) (c), and orientation (b) (d) energy landscapes for single superellipsoidal particle (n=r=4; r_x:r_y:r_z=2.5:1:10) between elliptical electrode configuration. Field conditions are for 2 V_{pp} and frequencies for (a) (b) 0.4 MHz and (c) (d) 2.0 MHz. Energy values greater than 10 kT are removed for a better visualization of the energy landscape. Sketches at the bottom represent the relative position and orientation of particle between the electrode.

There are three reasons why we finally design an elliptical electrode. First, to generate frequency dependent control, a similar configuration to parallel electrode is necessary. Secondly, the shape of the electrode will determine the shape of electric field in some extent, so an elliptical electrode will generate an electric field with

elliptical shape and restrict the ellipsoidal or superellipsoidal particle more firmly. The last reason is that, after tested of several configurations such as circle, square and rectangular, high aspect ratio will help to restrict particle in the center area. According to all the reasons above, an elliptical electrode with aspect ratio equals to 4 is designed and produced through micro-fabrication process.

In **Figure 20** (a) and (b), the particle is restricted at the central region and the long axis of the particle is oriented perpendicular to the *x*-component of the electric field. Under high frequency conditions, as shown in **Figure 20** (c) and (d), the particle is still located in the center but oriented parallel to the *x*-component of the electric field. This simulation results prove that the elliptical electrode has the ability to control single particle's position and orientation at the same time.

5. CONCLUSION

This work mainly focuses on the analyze of single anisotropic colloidal particle behavior under the influence of an AC electric field. The measured potential energy landscapes verify the simulation results of the particle equilibrium state under different electric field conditions (frequency and voltage) between parallel, quadrupole and octupole electrodes. The Parallel electrode configuration provides restriction on the particle orientation and position along two axes, while quadrupole electrode generates in-plane control of position, but particle can freely rotate in the center of the electrode gap. The simulated and experimental potential energy landscape of single particle between different electrode configurations improve the understanding of the positional and orientational trapping of anisotropic particles. Based on the results, a new electrode configuration was designed. The simulation analysis of electrode with superelliptical gap proves that new electrode could provide control on particle position and orientation simultaneously by tuning frequency and voltage. This research is not only expected to generate high dimensional control on single particle, but also has the potential in further particle assembly research. Furthermore, the procedure of producing fluorescent superellipsoidal particle is developed which could be the fundamental of experiments using Confocal microscope for 3D analysis of particle behavior within AC electric field.

The second part of this work revolves the dynamic analysis of superellipsoidal

particle between AC electric field. The expression of force and torque generated by AC electric field are developed, force and torque along different directions are calculated separately as a function of particle position and under different field conditions. The force and torque are also analyzed as a function of frequency and voltage. Force along the *z*-direction is normally balanced by electrostatic interaction and gravitational force; the result provides a method to estimate the magnitude of these interactions. The analysis of torque revolves interesting results, where the maximum torque along z direction (rotation of θ) is reached at 45°, different from general guess that maximum will appear at 0°. The relationship between energy landscape analysis and dynamic analysis are examined and perfectly matched.

The last part of the work introduces the concept of stiffness, which demonstrates the magnitude of the restriction generated by the AC electric field. Two different methods are applied to calculate the stiffness and the results of both are compared with experimental data, which show a good match. The stiffness of position and orientation as a function of frequency and voltage shows the possibility to control the stiffness precisely by tuning electric field conditions. This result could be useful in the future research of particle control and assembly.

6. REFERENCES

1 Lu, P. J. & Weitz, D. A. Colloidal Particles: Crystals, Glasses, and Gels. *Annual Review of Condensed Matter Physics* **4**, 217-233, doi:10.1146/annurev-conmatphys-030212-184213 (2013).

2 Matijevic, E. Monodispersed metal (hydrous) oxides-a fascinating field of colloid science. *Accounts of Chemical Research* **14**, 22-29 (1981).

3 Keville, K., Franses, E. & Caruthers, J. Preparation and characterization of monodisperse polymer microspheroids. *Journal of colloid and interface science* **144**, 103-126 (1991).

4 Rupp, B., Torres-Diaz, I., Hua, X. & Bevan, M. A. Measurement of Anisotropic Particle Interactions with Nonuniform ac Electric Fields. *Langmuir : the ACS journal of surfaces and colloids* **34**, 2497-2504, doi:10.1021/acs.langmuir.7b04066 (2018).

5 Pourjavadi, A., Fakoorpoor, S. M., Hosseini, P. & Khaloo, A. Interactions between superabsorbent polymers and cement-based composites incorporating colloidal silica nanoparticles. *Cement and Concrete Composites* **37**, 196-204 (2013).

6 Brun, N., Ungureanu, S., Deleuze, H. & Backov, R. Hybrid foams, colloids and beyond: From design to applications. *Chemical Society Reviews* **40**, 771-788 (2011).

7 Lettinga, M. P., Barry, E. & Dogic, Z. Self-diffusion of rod-like viruses in the nematic phase. *Europhysics Letters (EPL)* **71**, 692-698, doi:10.1209/epl/i2005-10127-x (2005).

8 Lee, K. J., Yoon, J. & Lahann, J. Recent advances with anisotropic particles. *Current Opinion in Colloid & Interface Science* **16**, 195-202, doi:10.1016/j.cocis.2010.11.004 (2011).

9 Glotzer, S. C. & Solomon, M. J. Anisotropy of building blocks and their assembly into complex structures. *Nature materials* **6**, 557-562, doi:10.1038/nmat1949 (2007).

10 Yang, S.-M., Kim, S.-H., Lim, J.-M. & Yi, G.-R. Synthesis and assembly of structured colloidal particles. *Journal of Materials Chemistry* **18**, 2177, doi:10.1039/b716393b (2008).

11 Torres-Diaz, I. & Bevan, M. A. General Potential for Anisotropic Colloid-Surface Interactions. *Langmuir : the ACS journal of surfaces and colloids* **33**, 4356-4365, doi:10.1021/acs.langmuir.7b00051 (2017).

12 Shah, A. A. *et al.* Liquid crystal order in colloidal suspensions of spheroidal particles by direct current electric field assembly. *Small* **8**, 1551-1562 (2012).

13 Champion, J. A., Katare, Y. K. & Mitragotri, S. Particle shape: a new design parameter for micro-and nanoscale drug delivery carriers. *Journal of controlled release* **121**, 3-9 (2007).

14 Gratton, S. E. *et al.* The effect of particle design on cellular internalization pathways. *Proceedings of the National Academy of Sciences of the United States of America* **105**, 11613-11618, doi:10.1073/pnas.0801763105 (2008).

15 Muro, S. *et al.* Control of endothelial targeting and intracellular delivery of therapeutic enzymes by modulating the size and shape of ICAM-1-targeted carriers. *Molecular therapy : the journal of the American Society of Gene Therapy* **16**, 1450-1458, doi:10.1038/mt.2008.127 (2008).

16 Ge, J., Neofytou, E., Cahill, T. J., 3rd, Beygui, R. E. & Zare, R. N. Drug release from electric-field-responsive nanoparticles. *ACS nano* **6**, 227-233, doi:10.1021/nn203430m (2012).

17 Nuñez, L. & Kaminski, M. D. Transuranic separation using organophosphorus extractants

adsorbed onto superparamagnetic carriers. *Journal of Magnetism and Magnetic Materials* **194**, 102-107, doi:10.1016/s0304-8853(98)00571-x (1999).

18 Bergemann, C., Müller-Schulte, D., Oster, J., à Brassard, L. & Lübbe, A. S. Magnetic ion-exchange nano- and microparticles for medical, biochemical and molecular biological applications. *Journal of Magnetism and Magnetic Materials* **194**, 45-52, doi:10.1016/s0304-8853(98)00554-x (1999).

19 Giri, S., Trewyn, B. G., Stellmaker, M. P. & Lin, V. S. Stimuli-responsive controlled-release delivery system based on mesoporous silica nanorods capped with magnetic nanoparticles. *Angewandte Chemie* **44**, 5038-5044, doi:10.1002/anie.200501819 (2005).

20 Grier, D. G. A revolution in optical manipulation. *Nature* **424**, 810-816, doi:10.1038/nature01935 (2003).

21 Juarez, J. J., Cui, J. Q., Liu, B. G. & Bevan, M. A. kT-scale colloidal interactions in high frequency inhomogeneous AC electric fields. I. Single particles. *Langmuir : the ACS journal of surfaces and colloids* **27**, 9211-9218, doi:10.1021/la201478y (2011).

22 Ramos, A., Morgan, H., Green, N. G. & Castellanos, A. The role of electrohydrodynamic forces in the dielectrophoretic manipulation and separation of particles. *Journal of Electrostatics* **47**, 71-81, doi:10.1016/s0304-3886(99)00031-5 (1999).

23 Gosse, C. & Croquette, V. Magnetic tweezers: micromanipulation and force measurement at the molecular level. *Biophysical journal* **82**, 3314-3329 (2002).

24 Cong, H., Chen, J. & Ho, H.-P. Trapping, sorting and transferring of micro-particles and live cells using electric current-induced thermal tweezers. *Sensors and Actuators B: Chemical* **264**, 224-233, doi:10.1016/j.snb.2018.02.016 (2018).

25 Vega-Bellido, G. I., DeLaCruz-Araujo, R. A., Kretzschmar, I. & Cordova-Figueroa, U. M. Self-assembly of magnetic colloids with shifted dipoles. *Soft Matter*, doi:10.1039/c8sm02591f (2019).

26 Mittal, M., Lobo, R. F. & Furst, E. M. Externally directed assembly of disk-shaped zeolite particles by an electric field. *Journal of Materials Research* **26**, 215-222 (2011).

27 Juárez, J. J., Feicht, S. E. & Bevan, M. A. Electric field mediated assembly of three dimensional equilibrium colloidal crystals. *Soft Matter* **8**, 94-103, doi:10.1039/c1sm06414b (2012).

28 Morgan, H. & Green, N. G. *AC electrokinetics*. (Research Studies Press, 2003).

29 Jones, T. Electromechanics of ParticlesCambridge Univ. *Press, Cambridge* (1995).

30 Miller, R. D. & Jones, T. B. Electro-orientation of ellipsoidal erythrocytes. Theory and experiment. *Biophysical Journal* **64**, 1588-1595, doi:10.1016/s0006-3495(93)81529-7 (1993).

31 Saito, M., Schwan, H. P. & Schwarz, G. Response of Nonspherical Biological Particles to Alternating Electric Fields. *Biophysical Journal* **6**, 313-327, doi:10.1016/s0006-3495(66)86659-6 (1966).

32 Neuman, K. C. & Nagy, A. Single-molecule force spectroscopy: optical tweezers, magnetic tweezers and atomic force microscopy. *Nature methods* **5**, 491-505, doi:10.1038/nmeth.1218 (2008).

33 Velev, O. D. & Gupta, S. Materials Fabricated by Micro- and Nanoparticle Assembly - The Challenging Path from Science to Engineering. *Advanced Materials* **21**, 1897-1905, doi:10.1002/adma.200801837 (2009).

34 Perez Garcia, L., Donlucas Perez, J., Volpe, G., A, V. A. & Volpe, G. High-performance

reconstruction of microscopic force fields from Brownian trajectories. *Nature communications* **9**, 5166, doi:10.1038/s41467-018-07437-x (2018).

35 Barr, A. H. Superquadrics and angle-preserving transformations. *IEEE Computer graphics and Applications* **1**, 11-23 (1981).

36 Consolo, G. Onset of linear instability driven by electric currents in magnetic systems: a Lagrangian approach. *Ricerche di Matematica* **65**, 413-422 (2016).

37 Evans, D. J. On the representatation of orientation space. *Molecular Physics* **34**, 317-325, doi:10.1080/00268977700101751 (2006).

38 Schiller, P., Kruger, S., Wahab, M. & Mogel, H. J. Interactions between spheroidal colloidal particles. *Langmuir : the ACS journal of surfaces and colloids* **27**, 10429-10437, doi:10.1021/la2015918 (2011).

39 White, L. R. On the deryaguin approximation for the interaction of macrobodies. *Journal of Colloid and Interface Science* **95**, 286-288, doi:10.1016/0021-9797(83)90103-0 (1983).

40 Jaklic, A., Leonardis, A. & Solina, F. *Segmentation and recovery of superquadrics*. Vol. 20 (Springer Science & Business Media, 2013).

41 Stratton, J. Electromagnetic Theory McGraw-Hill. *New York*, 31-434 (1941).

42 Morgan, H., Izquierdo, A. G., Bakewell, D., Green, N. G. & Ramos, A. The dielectrophoretic and travelling wave forces generated by interdigitated electrode arrays: analytical solution using Fourier series. *Journal of Physics D: Applied Physics* **34**, 1553 (2001).

43 Huang, Y. & Pethig, R. Electrode design for negative dielectrophoresis. *Measurement Science and Technology* **2**, 1142-1146, doi:10.1088/0957-0233/2/12/005 (1991).

44 Singh, S. & Dunmur, D. A. *Liquid crystals: fundamentals*. (World Scientific, 2002).

45 Han, Y. *et al.* Brownian Motion of an Ellipsoid. *Science* **314**, 626-630, doi:10.1126/science.1130146 (2006).

46 Bevan, M. A. & Eichmann, S. L. Optical microscopy measurements of kT-scale colloidal interactions. *Current Opinion in Colloid & Interface Science* **16**, 149-157, doi:10.1016/j.cocis.2010.12.006 (2011).

47 Torres-Diaz, I., Rupp, B., Yang, Y. & Bevan, M. A. Energy landscapes for ellipsoids in non-uniform AC electric fields. *Soft Matter* **14**, 934-944, doi:10.1039/c7sm02287e (2018).

48 Chang, D. E., Loire, S. & Mezi, I. Closed-form solutions in the electrical field analysis for dielectrophoretic and travelling wave inter-digitated electrode arrays. *Journal of Physics D: Applied Physics* **36**, 3073-3078, doi:10.1088/0022-3727/36/23/032 (2003).

49 Stratton, J. A. *Electromagnetic theory*. (John Wiley & Sons, 2007).

50 Keller, S., Blagoi, G., Lillemose, M., Haefliger, D. & Boisen, A. Processing of thin SU-8 films. *Journal of Micromechanics and Microengineering* **18**, 125020, doi:10.1088/0960-1317/18/12/125020 (2008).

51 SU-8 data sheet.

52 Tao, S. L., Popat, K. & Desai, T. A. Off-wafer fabrication and surface modification of asymmetric 3D SU-8 microparticles. *Nature protocols* **1**, 3153-3158, doi:10.1038/nprot.2006.451 (2006).

53 Tang, X., Zhang, J., Bevan, M. A. & Grover, M. A. A comparison of open-loop and closed-loop strategies in colloidal self-assembly. *Journal of Process Control* **60**, 141-151, doi:10.1016/j.jprocont.2017.06.003 (2017).

7. VITA

Name: Zhaonian Jia

Birth: June, 10, 1994, Beijing, China

Address: Zhaonian Jia may be contacted through Dr. M.A. Bevan at the Chemical and Biomolecular Engineering Department, Johns Hopkins University, Baltimore, MD 21218

Email Address: cloudyjzn@gmail.com

Education: B.Eng. & B.S., Molecular Science and Engineering, Tianjin University (joint program with Nankai University), 2016

Research: Research on synthesis and Properties of Novel Near Infrared Absorbing Dyes, with Dr. Zhijian Chen, Tianjin University, Tianjin, 2016